

國立交通大學
電機與控制工程學系

碩士論文

直流無刷馬達無感測驅動技術之實現



IMPLEMENTATION OF SENSORLESS DRIVE
TECHNOLOGY FOR THE BLDC MOTOR

研究生：程思穎

指導教授：陳永平 教授

中華民國九十五年六月

直流無刷馬達無感測驅動技術之實現

IMPLEMENTATION OF SENSORLESS DRIVE
TECHNOLOGY FOR THE BLDC MOTOR

研究生：程思穎

Student： Szu-Ying Cheng

指導教授：陳永平 教授

Advisor： Professor Yon-Ping Chen



碩士論文

A Thesis

Submitted to Department of Electrical and Control Engineering

College of Electrical and Computer Engineering

National Chiao Tung University

In Partial Fulfillment of the Requirements

For the degree of Master

In

Electrical and Control Engineering

June 2006

Hsinchu, Taiwan, Republic of China

中華民國九十五年六月

直流無刷馬達無感測驅動技術之實現

學生：程思穎

指導教授：陳永平 教授

國立交通大學電機與控制工程學系



因直流無刷馬達有高功率密度、高效率以及易控制的特性，使得近年來被廣泛的應用在日常生活中。控制直流無刷馬達一般傳統的方式都是依賴安裝在馬達內部的位置感測器或是編碼器，但是這些方式存在了一些不可避免的缺點，例如體積和成本的增加以及會受到馬達運轉溫度的影響等。因此，無感測控制的方式近年來成為越來越被重視以及研究的課題。本論文主要目的是分析並且實現直流無刷馬達無感測偵測元件之驅動器研製。反電動式位置偵測法被運用在即時回授的系統中，偵測出轉子磁極的位置，以提供換相訊號。此外，無感測最常見到的啟動問題，也藉由論文中所提到的起始位置偵測方式克服了。一旦起始位置被偵測出來之後，馬達便可有效率的由靜止啟動到要求的速度。這些無感測的控制方法以及由靜止啟動的過程將在實驗結果中完整呈現。

IMPLEMENTATION OF SENSORLESS DRIVE TECHNOLOGY FOR THE BLDC MOTOR


Student: Szu-Ying Cheng

Advisor: Professor Yon-Ping Chen

Department of Electrical and Control Engineering

National Chiao Tung University

ABSTRACT

The logo of National Chiao Tung University is a circular emblem with a gear-like outer border. Inside the circle, there is a stylized representation of a building or a bridge structure, with the letters 'NCTU' prominently displayed in the center. The logo is rendered in a blue color.

Nowadays, the BLDC motor becomes more and more attractive and be applied to many applications since it is easy to control and with high power density and high efficiency. Conventionally, the Hall-effect sensors are needed in electrical commutation. However, the Hall-effect sensors have several disadvantages, such as cost, size and reliability. Therefore, the sensorless control methods have been widely investigated in recent years. This thesis analyzes and then realizes a sensorless drive for the BLDC motor with the position estimated method to control the motor from standstill to the desired speed. In addition, the start-up problem existing in the back-EMF based method has been overcome simply by the initial position detection. Once the initial rotor position is attained, the motor can be driven from standstill effectively by a modified open-loop method. Finally, experimental results are included to demonstrate the success of the proposed sensorless control algorithm.

Acknowledgment

本論文能順利完成，首先感謝指導老師 陳永平教授這段期間來孜孜不倦的指導，讓作者在研究方法及英文寫作上有著長足的進步，在為學處事的態度上亦有相當的成長，謹向老師致上最高的謝意；感謝建峰學長平日在攻讀博士學位之餘，不吝傳授知識與經驗及給予建議，在此表達真摯地感謝；也謝謝欣達學長不遺餘力的把研究成果傳授給我。最後，感謝口試委員 楊谷洋老師以及 張浚林老師提供寶貴意見，使得本論文能臻於完整。

另外，還要感謝可變結構控制實驗室的豐洲學長、世宏學長、桓展學長、人中、宜穎、仲賢以及學弟妹們的陪伴，讓我在實驗室的研究生活充滿溫馨與快樂；也謝謝昌衢在我研究生活中不斷的給予我支持鼓勵以及陪伴。最後，感謝最親愛的家人們，爸爸、媽媽、姐姐怡禎以及弟弟奎皓，總是能夠給予我生活上的照顧與精神上的支持，讓我能夠積極快樂的度過求學生活。

謹以此篇論文獻給所有關心我、照顧我的人。

程思穎 2006.6

Contents

Chinese Abstract	i
English Abstract	ii
Acknowledgment	iii
Contents	iv
Index of Figures	vii
Index of Tables	xii

CHAPTER 1 INTRODUCTION	1
1.1 BACKGROUND	1
1.3 THESIS ORGANIZATION	2
CHAPTER 2 BASIC CONCEPTS OF BLDC MOTORS.....	4
2.1 CHARACTERISTICS OF BLDC MOTORS	4
2.2 MATHEMATICAL MODELING OF BLDC MOTORS.....	6
2.3 TYPICAL COMMUTATION PRINCIPLE.....	10
CHAPTER 3 SENSORLESS COMMUTATION CONTROL FOR BLDC MOTORS	16
3.1 REVIEW OF SENSORLESS CONTROL METHODS FOR BLDC MOTORS	17
3.1.1 Kalman-filter based method.....	17
3.1.2 Third-harmonics voltage based detection method	18
3.1.3 Free-Wheeling diode conducting method.....	21
3.2 BACK-EMF BASED POSITION ESTIMATION METHOD	24

3.2.1 Zero-crossing detection.....	25
3.2.2 Commutation phase shifter	28
CHAPTER 4 START-UP STRATEGY AND PROCEDURE FOR BLDC MOTORS.	32
4.1 START-UP STRATEGY	32
4.1.1 Open-loop start-up method	32
4.1.2 Inductive sense start-up method	33
4.2 START-UP PROCEDURE.....	37
4.2.1 Initial position detection	37
4.2.2 Start-up from standstill	41
CHAPTER 5 HARDWARE SETUP AND IMPLEMENTATION OF SENSORLESS	
DRIVES	45
5.1 EXPERIMENTAL SYSTEM DESCRIPTIONS	45
5.2 THE DRIVER CIRCUIT UNIT.....	48
5.3 THE SENSORLESS CONTROL UNIT	52
5.4 FILTER CIRCUIT UNIT	56
CHAPTER 6 EXPERIMENTAL RESULTS AND ANALYSIS.....	60
6.1 EXPERIMENTAL RESULTS OF THE COMMUTATION CONTROL.....	60
6.2 EXPERIMENT RESULTS OF THE START-UP PROCEDURE.....	68

CHAPTER 7 CONCLUSIONS75

REFERENCE.....77

APPENDIX.....81



Index of Figures

Fig.2.1	The basic configuration of BLDC motor.....	5
Fig.2.2	Equivalent modeling for a BLDC motor.....	6
Fig.2.3	Characteristic for co-energy	9
Fig.2.4	Ideal back-EMF and phase current waveform of a BLDC motor	11
Fig.2.5	System schematic of typical commutation control for a BLDC motor ...	12
Fig.2.6	The timing diagram of back-EMFs and Hall-effect signals	13
Fig.2.7	Two-phase conducting period and commutation period.....	15
Fig.3.1	Relationship between the back-EMFs, the third harmonic voltage and the rotor flux linkage.....	20
Fig.3.2	Free-wheeling conducting circuit in active signal S1 to S5.....	23
Fig.3.3	Free-wheeling diode conducting method: (a) current waveform in an open phase, (b) Diode conducting detecting circuit	24
Fig.3.4	Ideal three terminal voltages and the waveform of back-EMF	26
Fig.3.5	The relationship between the non-excited phase back-EMF and Hall-effect signals	27
Fig.3.6	System schematic of sensorless BLDC motor drive	28
Fig.3.7	Block diagram of simplified-type FIPS.....	30
Fig.3.8	The operational waveform of the proposed phase shifter	31

Fig.4.1	The flux linkage with positive or negative current.....	35
Fig.4.2	The responses of current with positive or negative direction.....	35
Fig.4.3	Current responses i_{1+} and i_{1-} to the rotor position	38
Fig.4.4	First difference of current responses to the rotor position.....	39
Fig.4.5	Second difference of current responses to the rotor position	40
Fig.4.6	The modified open-loop start-up method	41
Fig.4.7	The relation between the command signal and the circuit signal.....	44
Fig.4.8	The relation between the command signal and the circuit signal without initial position detection.....	44
Fig.5.1	The complete hardware PC-based control system.....	45
Fig.5.2	The block diagram of the xPC Target environment.....	47
Fig.5.3	The block diagram of driver circuit unit.....	48
Fig 5.4	The functional block diagram of IR2113.....	49
Fig.5.5	The typical connection of IR2113 to power MOSFET	50
Fig.5.6	The three phase motor driver circuit	51
Fig.5.7	The motor driver circuit.....	51
Fig.5.8	The block diagram of sensorless control unit.....	52
Fig.5.9	The ideal trapezoidal back-EMFs and torque production in a Y-connected three phase BLDC motor	54

Fig.5.10	PWM on the high side: (a) current during ON time, (b) Current during OFF time, (b) Current during OFF time	55
Fig.5.11	Frequency spectrum in a PWM signal.....	56
Fig.5.12	External low-pass filter.....	57
Fig.5.13	Bode plot of the external low-pass filter	58
Fig.5.14	The external low-pass filter circuit.....	59
Fig.6.1	The block diagram of overall sensorless control algorithm	60
Fig.6.2	The block diagram of frequency independent phase shifter (FIPS).....	61
Fig.6.3	Terminal voltage in a high angular velocity	62
Fig.6.4	Terminal voltage in a low angular velocity	62
Fig.6.5	Frequency spectrum of terminal voltage in a low angular velocity	63
Fig.6.6	Frequency spectrum of terminal voltage after using the low-pass filter .	63
Fig.6.7	Terminal voltage in a low angular velocity after using the low-pass filter	64
Fig.6.8	Sensorless control performance in a high angular velocity (I).....	65
Fig.6.9	Sensorless control performance in a high angular velocity (II)	65
Fig.6.10	Sensorless control performance in a low angular velocity (I).....	66
Fig.6.11	Sensorless control performance in a low angular velocity (II).....	66
Fig.6.12	Comparison of the sensorless signals and conventional Hall-effect signals	

	in high angular velocity	67
Fig.6.13	Comparison of the sensorless signals and conventional Hall-effect signals in low angular velocity	67
Fig.6.14	Measured the six current responses of an stationary rotor	69
Fig.6.15	The block diagram of start-up procedure	69
Fig.6.16	The open-loop start-up form sector 0	70
Fig.6.17	The difference between command sector and Back-EMF detected sector.	70
Fig.6.18	(a) The block diagram of the whole sensorless system and (b) the switch condition signal	72
Fig.6.19	Results from standstill to commutation mode at low angular velocity (I)	73
Fig.6.20	Results from standstill to commutation mode at low angular velocity (II)	73
Fig.6.21	Results from standstill to commutation mode at high angular velocity (I)..	74
Fig.6.22	Results from standstill to commutation mode at high angular velocity (II)	74
Fig. A.1	The current responses of the well-known six segments	83

Fig. A.2 The differences between the current i_n^+ and i_n^- 83

Fig. A.3 The differences between the current Δi_n 84

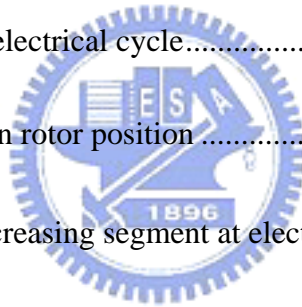
Fig.A.4 The torque generation of the six segments86

Fig.A.5 The pulse train and its response.....87



Index of Tables

Table 2.1 Position based of six segments with Hall-effect sensors signals.....	14
Table 4.1 Six segments of an electrical cycle.....	38
Table 4.2 Polarity of ddi on rotor position	40
Table 4.3 The definition of the position sector.....	43
Table 4.4 The relation between the duty ratio and estimated angular velocity	43
Table 5.1 The specification of the BLDC motor	46
Table 5.2 The phase commutation sequence.....	53
Table A.1 Six segments of an electrical cycle.....	82
Table A.2 Polarity of ΔI_{i_k} on rotor position	84
Table A.3 The exciting and increasing segment at electrical angle	87



Chapter 1

Introduction

1.1 Background

Nowadays, BLDC motors become more and more attractive for many industrial applications, such as electrical vehicles, compressors and DVD players etc. Comparing with other motors, BLDC motors possess some distinct advantages such as high torque, high power density and high efficiency. Since BLDC motors use permanent magnet for excitation, rotor position sensors are needed to perform electrical commutation. Conventionally, three Hall-effect sensors are used as rotor position sensors for BLDC motors. However, the sensors lead to several disadvantages, such as cost, size and reliability. In addition, the sensors may be sensitive to the motor temperature inside. Therefore, the sensorless control methods have been widely studied in recent years, such as back-EMF based position estimation method [1]-[3], third harmonic voltage position detection method [5], free-wheeling diode conducting method [6], and Kalman-filter method [4]. The first two methods both use the detected back-EMFs which should be measured at the instant of the unexcited phase. The third method, free-wheeling diode conducting method, uses indirect sensing of the zero-crossing of the back-EMFs to obtain the switching instants of BLDC motors. The Kalman-filter method is a stochastic observer in the least-square sense for estimating the states of

dynamic non-linear systems and it is viable for the on-line determination of the rotor position and velocity of a motor.

Among these control methods, the back-EMF based position estimation method is often used since the back-EMFs could be measured indirectly from the motor's terminal voltages. When a motor is running, back-EMF is induced in the coil, and the position information of a rotor can be detected by the back-EMF. However, back-EMF is only generated while a motor is running, which requires another initial position detection and start-up algorithm when a motor is at standstill or at low speed with insufficient back-EMF. Many researchers have focused on the open-loop start-up method [6] and inductive sense start-up method [10]-[11]. In this thesis, the detailed realization issues of the sensorless algorithm will be introduced, and be implemented by using a PC-based feedback control system. In addition, the start-up problem will be overcome in the experiment.

1.2 Thesis Organization

The thesis is organized as follows. First, the basic concepts of BLDC motors are introduced in Chapter 2, including the characteristics, mathematical modeling and commutation principle of BLDC motors. Among them, the commutation principle would focus on the conventional electrical commutation with Hall-effect sensors.

In Chapter 3, some sensorless control method will be introduced. First, Kalman-filter based method, third-harmonics voltage position detection method, and free-wheeling diode conducting method will be described. Then the back-EMF based position estimation method used in experiment will be introduced in detail.

Chapter 4 will discuss the start-up strategies, such as open-loop start-up method and inductive sense start-up method. The initial position of the rotor will be detected to avoid the temporary reverse rotation. An additional modified open-loop start-up method will be proposed to solve the start-up problem. Then the start-up procedure used in the implementation will be presented, including initial position detection and start-up from standstill.



Chapter 5 will describe the hardware setup and implementation of sensorless drive. The sensorless control method and start-up method are implemented by the software, Matlab[®]-Simulink[®]. This toolbox can help designer establish them easily and directly. Besides, the hardware circuit which is included in the driver circuit and filter circuit is set up by Real-Time workshop[®] (RTW) of Matlab[®]. The main idea of the hardware circuit is to realize and verify the sensorless control method. Chapter 6 will show the experimental results to demonstrate the success of BLDC motor drive. Finally, Chapter 7 gives the conclusions.

Chapter 2

Basic Concepts of BLDC Motors

A brushless DC (BLDC) motor is a rotating electric machine where the stator is a classic three-phase stator like that of an induction motor and the rotor has surface-mounted permanent magnets. In this chapter, the basic configuration and the characteristics of BLDC motors will be described in Section 2.1. Then the mathematical modeling will be represented in Section 2.2. Furthermore, a BLDC motor requires an inverter and a position sensor to perform “commutation” because a permanent magnet synchronous motor takes the place of dc motor with brushes and commutators [8]. Thus, the detail commutation and excited procedure will be illustrated in Section 2.3.



2.1 Characteristics of BLDC Motors

In general, a BLDC motor consists of a permanent magnet synchronous motor that converts electrical energy to mechanical energy. The basic configuration of BLDC motors are shown in Fig.2.1. In this figure, it's clear to see that and the excitation of BLDC motors which consists of permanent magnets is on the rotor and the armature is on the stator. On the other hand, BLDC motors come in 2-phase, 3-phase and 4-phase configuration. Corresponding to its type, the stator has the same numbers of windings.

Out of these, 3-phase motors are the most popular and widely used since 2-phase and 4-phase motors are usually used in small power condition [22]. Furthermore, the hall elements are installed inside the stator to detect the rotor position. Since the 3-phase BLDC motors have three windings which are distributed with 120° in electrical degree apart to each other, the driver structure including the six-step inverters using PWM signals. Thus, the principle of switching is based on electrical angular position information, which is decoded by three Hall-effect sensors.

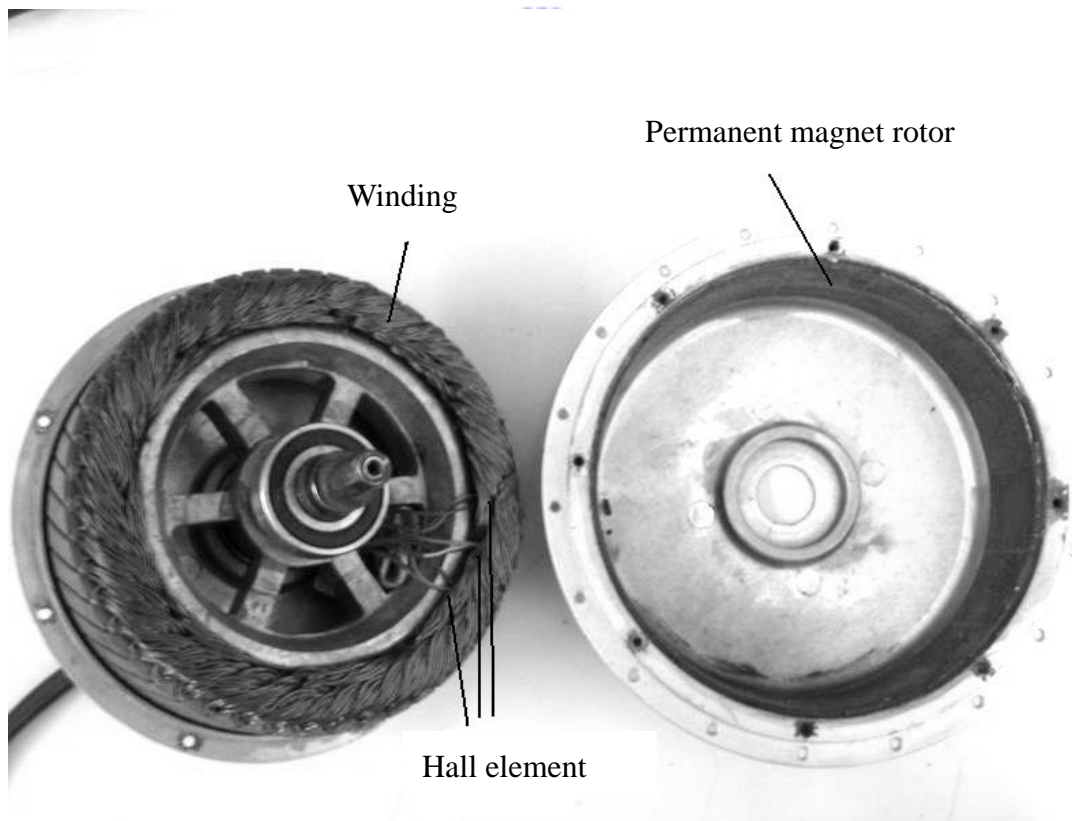


Fig.2.1 The basic configuration of BLDC motors

2.2 Mathematical Modeling of BLDC Motors

In general, a BLDC motor has a permanent-magnet rotor and its stator windings are wound to generate the trapezoidal back electromotive force (back-EMF), and thus it requires rectangular-shaped stator phase current to produce constant torque. Besides, the two-axis transformation (d, q model) [9], [22], commonly used in PMSM, is not necessary the best choice for modeling and simulating the BLDC motors.

The dynamic equations of BLDC motors with Y-connected stator windings are shown in Fig.2.2. When the neutral point is isolated, the phase currents of BLDC, $i_{as}(t)$,

$i_{bs}(t)$, and $i_{cs}(t)$, can be expressed as

$$i_{as}(t) + i_{bs}(t) + i_{cs}(t) = 0 \quad (2-1)$$

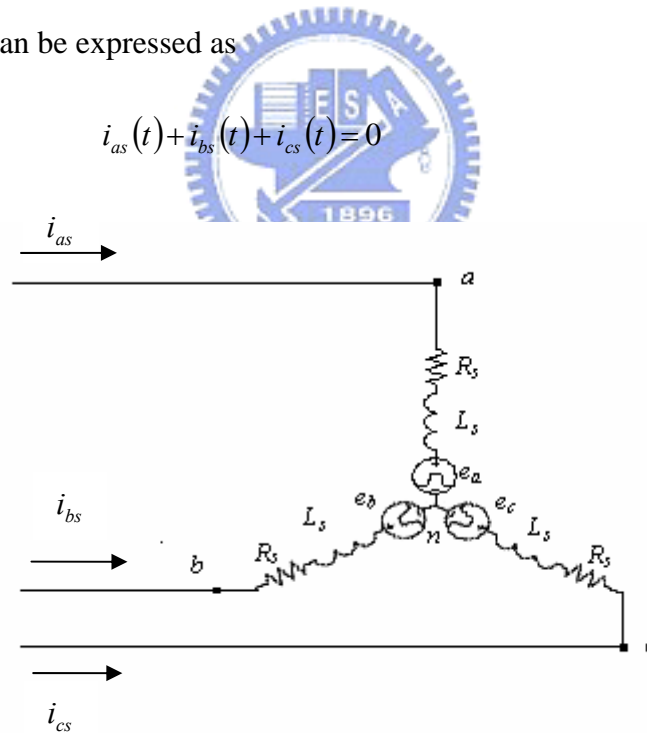


Fig.2.2 Equivalent modeling for a BLDC Motor

Because the three windings are distributed with $\frac{2\pi}{3}$ in electrical degree apart to each other, the stator current in vector space is generally represented as

$$I_s(t) = i_{as}(t) + i_{bs}(t)e^{j\frac{2\pi}{3}} + i_{cs}(t)e^{j\frac{4\pi}{3}} \quad (2-2)$$

where $i_{as}(t)$, $i_{bs}(t)e^{j\frac{2\pi}{3}}$, and $i_{cs}(t)e^{j\frac{4\pi}{3}}$ are the three phase currents correspondingly.

Let $\lambda_{as}(\theta_e, t)$, $\lambda_{bs}(\theta_e, t)$ and $\lambda_{cs}(\theta_e, t)$ be the fluxes related to the three phases of the stator, expressed as

$$\lambda_{as}(\theta_e, t) = L_s i_{as}(t) + L_{ms} i_{bs}(t)e^{j\frac{2\pi}{3}} + L_{ms} i_{cs}(t)e^{j\frac{4\pi}{3}} + \lambda_{pm} e^{j\theta_e} \quad (2-3)$$

$$\lambda_{bs}(\theta_e, t) = L_{ms} i_{as}(t)e^{-j\frac{2\pi}{3}} + L_s i_{bs}(t) + L_{ms} i_{cs}(t)e^{j\frac{2\pi}{3}} + \lambda_{pm} e^{j\left(\theta_e - \frac{2\pi}{3}\right)} \quad (2-4)$$

$$\lambda_{cs}(\theta_e, t) = L_{ms} i_{as}(t)e^{-j\frac{4\pi}{3}} + L_{ms} i_{bs}(t)e^{-j\frac{2\pi}{3}} + L_s i_{cs}(t) + \lambda_{pm} e^{j\left(\theta_e - \frac{4\pi}{3}\right)} \quad (2-5)$$

where L_{ms} and L_s respectively represent the mutual inductance and the self-inductance of the stator. Besides, λ_{pm} is the flux magnitude produced by the permanent magnets, which are assumed sinusoidally distributed in the air-gap.

With a cylindrical stator, the self-inductances of the field windings are independent of the rotor position θ when the harmonic effects of stator slot openings are neglected. Hence, the self-inductance L_s is constant, commonly further decomposed as

$$L_s = L_{ss} + L_{ls} \quad (2-6)$$

where L_{ss} takes into account the space-fundamental component of air-gap flux and L_{ls} is corresponding to the field-leakage flux.

The mutual inductances can be found on the assumption that the mutual inductance is due solely to space-fundamental air-gap flux. Because the phases are

displayed by $\frac{2\pi}{3}$ and $\cos(\pm\frac{2\pi}{3}) = -\frac{1}{2}$, the mutual inductances are

$$L_{ms} = -\frac{1}{2}L_{ss} \quad (2-7)$$

The phase-*a* flux linkage (2-3) can be rewritten as

$$\lambda_{as}(\theta_e, t) = (L_{ss} + L_{sl})i_{as}(t) - \frac{1}{2}L_{ss}(i_{bs}(t) + i_{cs}(t)) + \lambda_{pm} \cos \theta_e \quad (2-8)$$

With balanced three-phase currents, substitution of (2-1) gives

$$\lambda_{as}(\theta_e, t) = \left(\frac{3}{2}L_{ss} + L_{sl}\right)i_{as} + \lambda_{pm} \cos \theta_e \quad (2-9)$$

Based on the stator flux in (2-3)-(2-5) and (2-9), the stator voltages, $v_{as}(t)$, $v_{bs}(t)$, and

$v_{cs}(t)$, can be formulated as

$$v_{as}(t) = R_s i_{as}(t) + \frac{d}{dt} \lambda_{as}(\theta_e, t) = R_s i_{as}(t) + L \dot{i}_{as}(t) - \omega_e \lambda_{pm} \sin \theta_e \quad (2-10)$$

$$v_{bs}(t) = R_s i_{bs}(t) + \frac{d}{dt} \lambda_{bs}(\theta_e, t) = R_s i_{bs}(t) + L \dot{i}_{bs}(t) - \omega_e \lambda_{pm} \sin\left(\theta_e - \frac{2}{3}\pi\right) \quad (2-11)$$

$$v_{cs}(t) = R_s i_{cs}(t) + \frac{d}{dt} \lambda_{cs}(\theta_e, t) = R_s i_{cs}(t) + L \dot{i}_{cs}(t) - \omega_e \lambda_{pm} \sin\left(\theta_e - \frac{4}{3}\pi\right) \quad (2-12)$$

or in matrix form as

$$\mathbf{V}_{abcs} = R_s \mathbf{I}_{abcs} + L \dot{\mathbf{I}}_{abcs} - \omega_e \lambda_{pm} \begin{bmatrix} \sin \theta_e \\ \sin\left(\theta_e - \frac{2}{3}\pi\right) \\ \sin\left(\theta_e - \frac{4}{3}\pi\right) \end{bmatrix} \quad (2-13)$$

where $L = \frac{3}{2}L_{ss} + L_{sl}$, $\mathbf{V}_{abcs} = \begin{bmatrix} v_{as} \\ v_{bs} \\ v_{cs} \end{bmatrix}$, $\mathbf{I}_{abcs} = \begin{bmatrix} i_{as} \\ i_{bs} \\ i_{cs} \end{bmatrix}$, and ω_e is electrical angular

velocity.

Besides, since the rotor would be engaged by the excited phase, the torque of a

motor is produced in this moving process. The equation of the instant torque could be shown as

$$T_e(i_{as}, i_{bs}, i_{cs}, \theta_e) = \frac{\partial W_{co}}{\partial \theta_e} \quad (2-14)$$

where W_{co} is the co-energy defined in Fig.2.3, and represented as

$$W_{co} = \int \lambda_{as} di_{as} + \int \lambda_{bs} di_{bs} + \int \lambda_{cs} di_{cs} \quad (2-15)$$

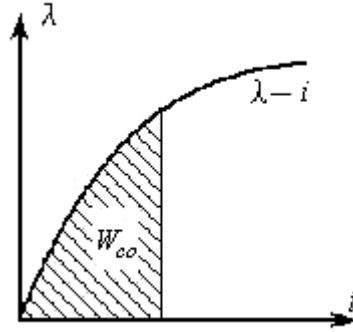


Fig.2.3 Characteristic for co-energy

In general, for a p-pole 3-phase motor, the total electrical energy could be shown as

$$\begin{aligned} W_{co} = & \frac{p}{2} \frac{1}{2} [L_s i_{as}^2 + L_s i_{bs}^2 + L_s i_{cs}^2] + \frac{p}{2} [L_{ms} i_{as} i_{bs} + L_{ms} i_{bs} i_{cs} + L_{ms} i_{as} i_{cs}] \\ & + \frac{p}{2} \lambda_{pm} \left[\cos(\theta_e) i_{as} + \cos\left(\theta_e - \frac{2}{3}\pi\right) i_{bs} + \cos\left(\theta_e - \frac{4}{3}\pi\right) i_{cs} \right] \end{aligned} \quad (2-16)$$

From (2-14) and (2-16), the electromagnetic torque would be formulated by three

phase currents, given as

$$T_e = -\frac{p}{2} \lambda_{pm} \left[\sin(\theta_e) i_{as} + \sin\left(\theta_e - \frac{2}{3}\pi\right) i_{bs} + \sin\left(\theta_e - \frac{4}{3}\pi\right) i_{cs} \right] \quad (2-17)$$

Then the back-EMFs could be shown in matrix form from (2-13) as

$$\begin{bmatrix} e_a \\ e_b \\ e_c \end{bmatrix} = \frac{d}{dt} \begin{bmatrix} \cos \theta_e \\ \cos \left(\theta_e - \frac{2}{3} \pi \right) \\ \cos \left(\theta_e - \frac{4}{3} \pi \right) \end{bmatrix} = -\omega_e \lambda_{pm} \begin{bmatrix} \sin \theta_e \\ \sin \left(\theta_e - \frac{2}{3} \pi \right) \\ \sin \left(\theta_e - \frac{4}{3} \pi \right) \end{bmatrix} \quad (2-18)$$

where e_a , e_b , and e_c are the phase back-EMFs. From (2-17) and (2-18), the relationship

between electromagnetic torque and back-EMFs could be represented as

$$T_e = \frac{p}{2} \frac{e_a i_{as} + e_b i_{bs} + e_c i_{cs}}{\omega_e} \quad (2-19)$$

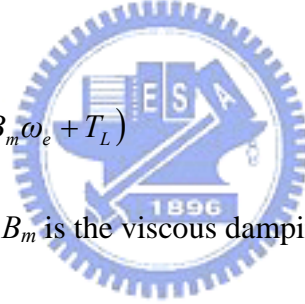
According to the Newton law, the electromechanical equation can be expressed as

$$T_e - \frac{2}{p} (+ B_m \omega_e + T_L) = \frac{2}{p} (J \dot{\omega}_e) \quad (2-20)$$

which could be rearranged as

$$T_e = \frac{2}{p} (J \dot{\omega}_e + B_m \omega_e + T_L) \quad (2-21)$$

where J is the motor's inertia, B_m is the viscous damping, T_L is the load torque



2.3 Typical Commutation Principle

The model of the 3-phase Y-connected BLDC motor consists of winding resistances, winding inductances, and back-EMF voltage sources [23]. The typical commutation for a BLDC motor is accomplished by controlling the six inverter switches according to the six-step sequence to produce the phase current waveforms as shown in Fig.2.4. Ideally, the currents are in rectangular shapes, and the stator inductance voltage drop may be neglected [7]. Thus, the sequence of the conducting

phase will be shown in Table 2.1 from Fig.2.4.

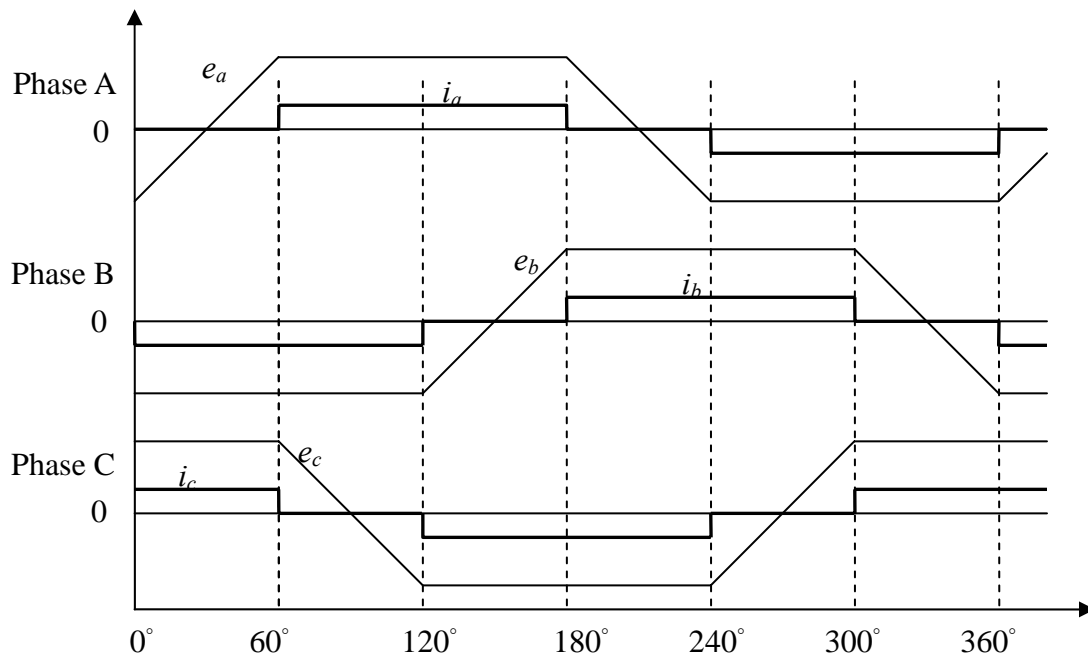


Fig.2.4 Ideal back-EMF and phase current waveform of a BLDC motor

The accurate rotor position sensors are required since the torque production performance largely depends on the relationship between excitation currents and back-EMFs. The rotor position sensing can be achieved by using the Hall-effect sensors for low-cost applications, or by resolving and optical encoders for high-performance applications. In reality, Hall-effect sensors are used most widely for electronic commutation of BLDC motor drives. Fig.2.5 shows the system schematic block diagram of the commutation control for a BLDC motor. This figure is included of the inverter circuit, the equivalent model of a BLDCM, and the feedback the signals of Hall-effect sensor.

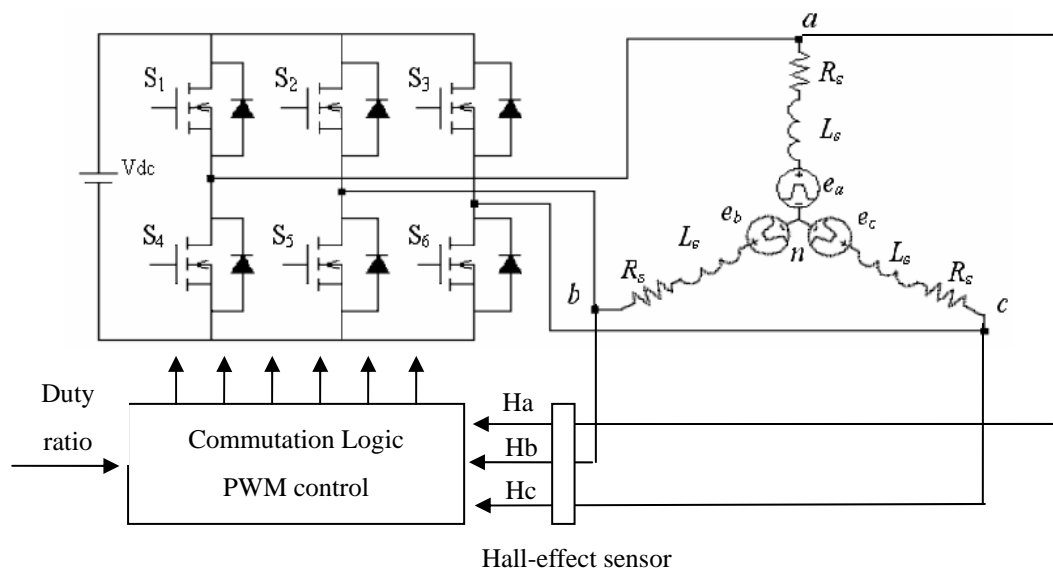


Fig.2.5 System schematic of typical commutation control for a BLDC motor

The inverter circuit of single-phase is cascaded by two power transistors, such as MOSFETs or IGBTs, as the active elements. Both of them can not conduct at the same time to avoid burning under over-current. Generally, NMOSFETs are selected to be the power transistors for small power motors. Based on the devices characteristics, to turn ON the NMOSFETs, a high gate voltage should be applied [21]. In addition, the six segments are processed in order, which is implemented by the six-step drive.

Generally, the typically commutation is based on the rotor position which is measured by three Hall-effect sensors located in the motor. The Hall-effect signals which would send the position messages are related to the back-EMFs . When the phase back-EMF is through the positive zero-crossing, its Hall signal will become high after 30° delay. On the contrary, when the phase back-EMF is through the negative

zero-crossing, its Hall signal will become low after 30° delay. The timing diagram of back-EMFs and Hall-effect signals are shown in Fig.2.6.

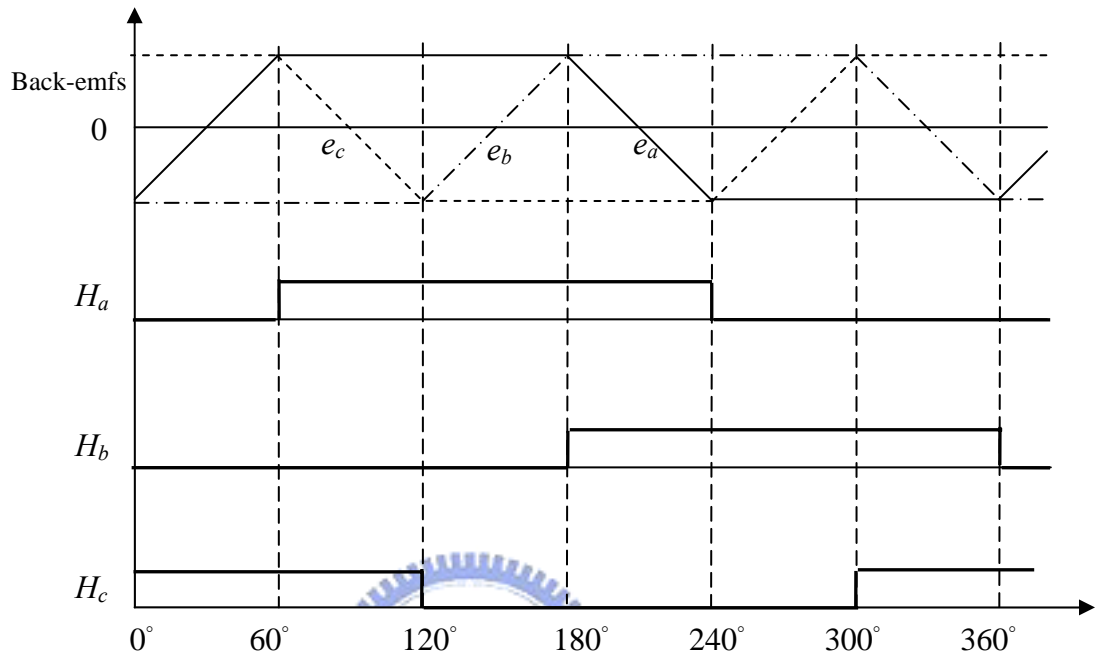


Fig.2.6 The timing diagram of back-EMFs and Hall-effect signals

Since the BLDC motor should be separated in six segments, the three Hall-effect sensors can produce digital signals in three bits as shown in Table 2.1. In the traditional control experiment, it is easy to know the rotor position and velocity because it just decodes the digital signals from Hall-effect sensors and differential the variance of one digital signal.

Table 2.1 Position based of six segments with Hall-effect sensors signals

Electrical angle	segment	Switch on	Hall-effect
$0^\circ \sim 60^\circ$	$C\bar{B}$	S_3, S_5	001
$60^\circ \sim 120^\circ$	$A\bar{B}$	S_1, S_5	101
$120^\circ \sim 180^\circ$	$A\bar{C}$	S_1, S_6	100
$180^\circ \sim 240^\circ$	$B\bar{C}$	S_2, S_6	110
$240^\circ \sim 300^\circ$	$B\bar{A}$	S_1, S_4	010
$300^\circ \sim 360^\circ$	$C\bar{A}$	S_3, S_4	011

Ideally, the conducted current waveforms are in rectangular shapes because only two phases are excited at any instant and the effect of free-wheeling diodes is ignored. Hence, the phase current can not be changed suddenly because the inductance exists. In order to analyze the characteristics during the phase commutation, the commutation from phase $a-c$ to phase $a-b$ is considered as an example. First, the diode S_1 and S_6 in Fig.2.5 will be conducted so that the current of the phase b will pass through the diode. Immediately after switching off Q_6 , the current of the phase b still pass through the diode until decaying to zero as shown in Fig.2.7. Hence, there exists commutation period between the two-phase conduction period. On the other hand, during the two-phase conducting period, two conducting phase currents are opposite and another one is zero. Therefore, the sum of three phase currents will still equal to zero at any time.

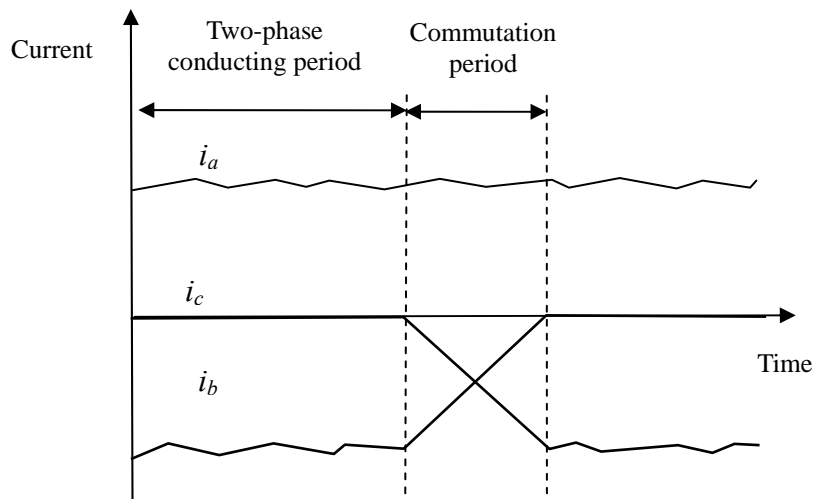


Fig.2.7 Two-phase conducting period and commutation period



Chapter 3

Sensorless Commutation Control for BLDC Motors

Since BLDC Motors use permanent magnets for excitation, rotor position sensors are needed to perform electrical commutation. Commonly, three Hall-effect sensors installed inside the BLDC motor are used to detect rotor position. However, the rotor position sensors present several drawbacks from the viewpoint of total system cost, size, and reliability. Therefore, recent investigators have paid more and more attentions to sensorless control without any Hall-effect sensors and proposed many sensorless-related technologies.

Section 3.1 introduces three sensorless control methods. Besides, back-EMF based position detection is more useful than others since the back-EMFs proportional to the rotating angular velocity should be recognized directly or indirectly and the hardware could be realized easily. Hence the back-EMF based position detection will be narrowly described clearly in Section 3.2.



3.1 Review of Sensorless Control Methods for BLDC Motors

Since the knowledge of six commutation instants per electrical is only needed for BLDC motors. In order to reduce cost and motor size, the elimination of the rotor position sensors is a very desirable objective in many applications. Furthermore, the sensorless control is the only way for some applications and many methods via sensorless control have been researched, such as back-EMF based position estimation method [1], [2], [3], [19], Kalman-filter based method [4], third-harmonics voltage position detection method [5], and free-wheeling diode conducting method [6]. More details about back-EMF based position estimation method will be discussed in Section

3.2.



3.1.1 Kalman-filter based method

A method which uses the extended Kalman filter (EKF) to estimate speed and rotor position of a BLDC motor is illustrated in [4]. The estimation algorithm is based on the state-space model of the motor and a statistical description of the uncertainties which is modeled by covariance matrices, including $P(t)$, $Q(t)$, and $R(t)$. Define that $P(t)$ is for the system state vector, $Q(t)$ is for the model uncertainty, and $R(t)$ is for the measurement uncertainty.

Since the EKF is an efficient state estimator for nonlinear system and consists of

the prediction and correlation equations, the drive system could be described as

$$\dot{x}(t) = f[x(t), u(t), t] + n(t) \quad (3-1)$$

where the initial state vector $x(t_0)$ is modeled as a Gaussian random vector with mean x_0 and covariance P_0 , while $n(t)$ is a zero-mean white Gaussian noise independent of $x(t_0)$ and with a covariance matrix $Q(t)$. The measurement are modeled as

$$y(t_i) = h[x(t_i), t_i] + v(t_i) \quad (3-2)$$

where $v(t_i)$ is a zero-mean white Gaussian noise independent of $x(t_0)$ and with a covariance matrix $R(t_i)$. Hence, the EKF would generate a minimum-variance estimator since it has a predictor-corrector structure.

However, there exists a critical part since the design is to use accurate initial value for the various covariance matrices. In principle, these initial matrices need to be obtained by considering the stochastic properties of the corresponding noises. Since these noises are usually unknown, trial-and-error method is used for tuning the initial estimates of these matrices to obtain the best tradeoff between filter stability and convergence time.

3.1.2 Third-harmonics voltage based detection method

This method in [5] deals with the use of the third harmonic component of the back-EMF for indirect sensing the rotor flux position. The six step inverters switch the

stator excitation at every $\pi/3$ electrical degree. The switching can be detected by monitoring the third-harmonic voltage of the back-EMF. The stator voltage equation for phase a , for instance, is written as

$$v_{as} = R_s i_{as} + L_s \frac{d}{dt}(i_{as}) + e_{as} \quad (3-3)$$

Similar expressions can be written for the other two stator phases. The phase stator resistance and inductance are represented as R_s and L_s respectively. The term e_{as} represents the back-EMF voltage. For a full pitch magnet and full pitch stator phase winding, the back-EMF voltages contains the following frequency components

$$e_{as} = E(\cos\omega_e t + k_3 \cos 3\omega_e t + k_5 \cos 5\omega_e t + k_7 \cos 7\omega_e t + \dots) \quad (3-4)$$

$$e_{bs} = E(\cos(\omega_e t - 2\pi/3) + k_3 \cos 3(\omega_e t - 2\pi/3) + \dots) \quad (3-5)$$

$$e_{cs} = E(\cos(\omega_e t + 2\pi/3) + k_3 \cos 3(\omega_e t + 2\pi/3) + \dots) \quad (3-6)$$

Because of Y-connected stator windings, the third-harmonic voltage component at the terminal voltage is only due to the back-EMF. The summation of the three stator phase voltages is a zero sequence which contains a dominant third-harmonic component and high frequency components, expressed as

$$v_{an} + v_{bn} + v_{cn} = 3Ek_3 \cos 3\omega_e t + v_{high_freq} = v_3 + v_{high_freq} \quad (3-7)$$

where v_3 is the third-harmonic voltage and v_{high_freq} is the high frequency components.

Therefore, the rotor flux can be estimated from this third-harmonic signal by integrating the resultant voltage v_3 ,

$$\lambda_{r3} = \int v_3 dt \quad (3-8)$$

Since the third harmonic flux linkage lags the third harmonic of the back-EMF voltages by 30 degrees, the commutation signals can be obtained by directly detecting the zero-crossing of the third harmonic flux linkage without any phase delay. Fig.3.1 shows the relationship between the back-EMFs, the third harmonic voltage and the rotor flux linkage; it is clearly to see that the zero-crossing of λ_{r3} is the commutation instant. The result of the summation of the three phase voltages contain the third-harmonic voltage and high frequency sequence components that can be easily eliminated by a low-pass filter.

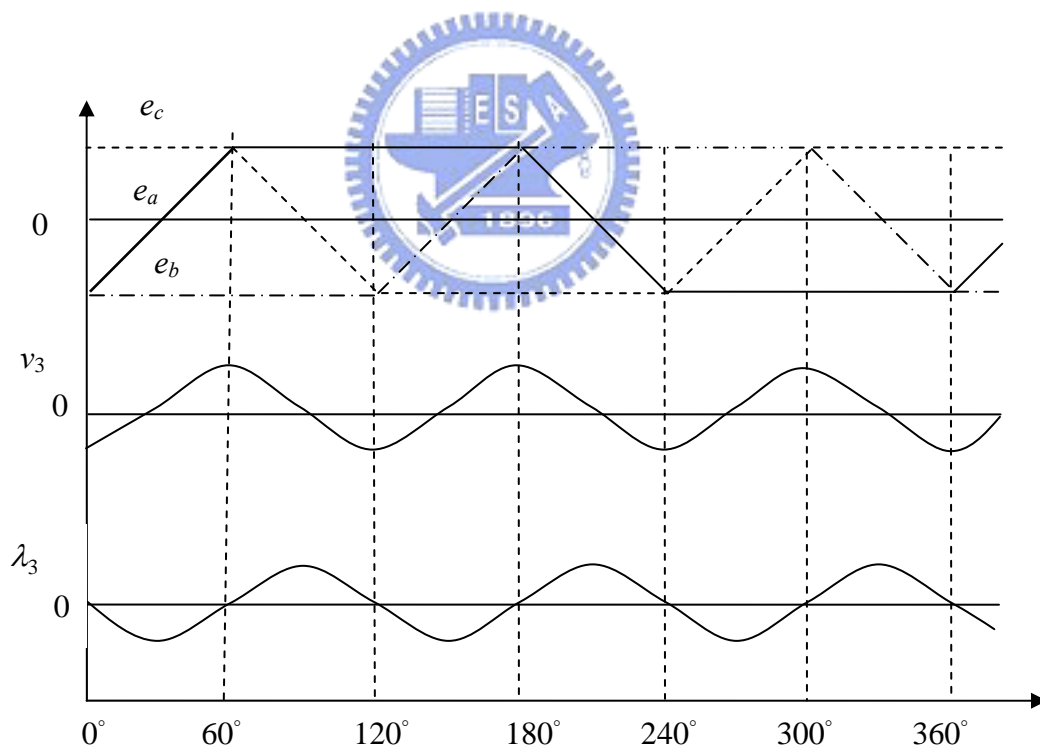


Fig.3.1 Relationship between the back-EMFs, the third harmonic voltage and the rotor flux linkage

To sum up, the important advantages of this method are easy to implementation

and low susceptibility to electrical noise. On the other hand, signal detection at low speeds with this method is possible because the third harmonic signal has a frequency three times higher than the fundamental back-EMF, allowing operation in a wider speed range than techniques based on sensing the motor back-EMF. However, it is difficult to sense the neutral point voltage. Therefore, the neutral terminal is not available due to the cost and structure constrains in application.

3.1.3 Free-Wheeling diode conducting method

Since the back-EMF is quite small and hard to detect during the low-speed operation, it is difficult to precisely detect the rotor position based on the back-EMF only. Recently, some approaches have included other information besides back-EMF to detect the rotor position, for example the work by S. Ogasawara and H. Akagi [6]. Their approach proposed a method on the basis of the conducting state of free-wheeling diodes connected with power transistors. Fig.3.2 shows the circuit with phase *a-b* conducted, which means the active signal is given to S1 and S5. If S1 is on state, the dc link voltage increases the main current *i*. If S1 turn off, the current *i* continues to flow through the free-wheeling diode D4 and decreases. Then, the voltage equation of this loop can be derived as

$$V_F + L_S \frac{di}{dt} + R_S i + e_a - e_b + R_S i + L_S \frac{di}{dt} + V_{CE} = 0 \quad (3-9)$$

where V_{CE} and V_F denote the forward voltage drop of the transistors and diode. From

(3-9), the voltage drop of the motor winding as

$$R_S i + L_S \frac{di}{dt} = -\frac{e_a - e_b}{2} - \frac{V_{CE} - V_F}{2} \quad (3-10)$$

The neutral voltage v_n which also shown in Fig.3.2, is given by

$$v_n = V_{CE} + R_S i + L_S \frac{di}{dt} - e_b = -V_F - R_S i - L_S \frac{di}{dt} - e_a \quad (3-11)$$

Substitution (3-10) into (3-11) gives the following equation

$$v_n = \frac{V_{CE} - V_F}{2} - \frac{e_a + e_b}{2} \quad (3-12)$$

Since the c -phase terminal voltage v_c equals $e_c + v_n$, v_c is given as

$$v_c = e_c + v_n = e_c + \frac{V_{CE} - V_F}{2} - \frac{e_a + e_b}{2} \quad (3-13)$$

Equation (3-13) holds good even in transient states because no motor constant are included. The conducting condition of the diode D6 is given by

$$v_c < -V_F \quad (3-14)$$

Substituting (3-13) into (3-14) gives the following equation

$$e_c - \frac{e_a + e_b}{2} < -\frac{V_{CE} + V_F}{2} \quad (3-15)$$

Since the back-EMF are assumed in ideal trapezoidal waveform, $e_a + e_b$ is approximately zero near the zero point of e_c . Therefore, the conducting condition of

D6 is given by

$$e_c < -\frac{V_{CE} + V_F}{2} \quad (3-16)$$

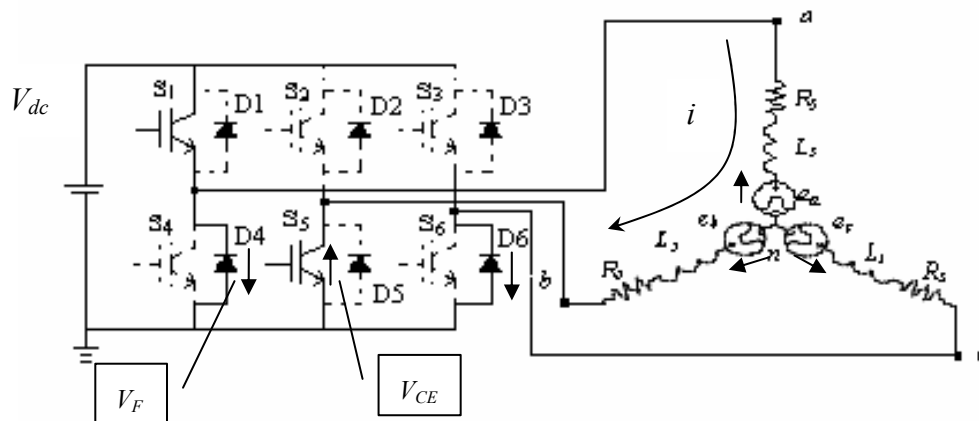


Fig.3.2 Free-wheeling conducting circuit in active signal S1 to S5

In general, V_{CE} and V_F are much smaller than the back-EMF. When the back-EMF e_c become negative, the open-phase current flows through the negative-sign diode D6.

Therefore, the zero-crossing point of the non-excited phase back-EMF can be equivalently obtained by detecting corresponding diode conducting condition.

Fig.3.3(a) shows a current waveform in an open phase, and Fig.3.3(b) shows a

specially designed circuit to detect whether the free-wheeling diodes are conducting or

not. A resistor and a diode are connected to a comparator for voltage clamping. The

reference voltage V_{ref} is slightly smaller than the forward voltage V_F drop of the

free-wheeling diode. After detecting the diode conducting instant in the non-excited

phase, a digital phase shifter is realized to generate the correct commutation signal.

However, the detecting circuit needs two isolated power supplies and the external

hardware circuit is required.

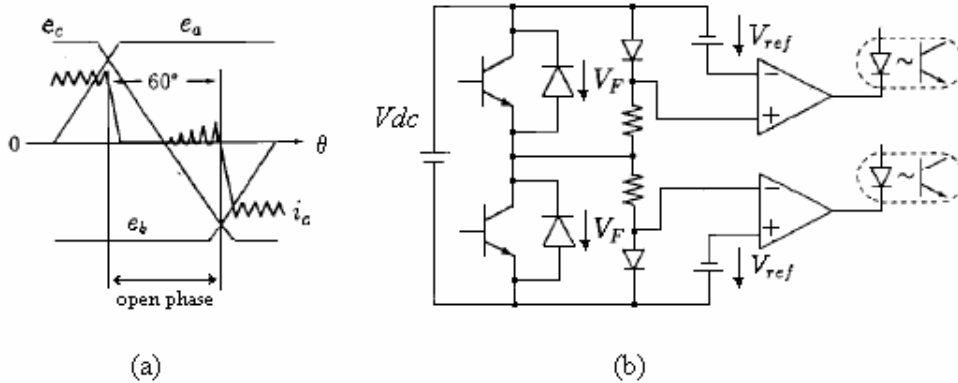


Fig.3.3 Free-wheeling diode conducting method: (a) current waveform in an open phase, (b) Diode conducting detecting circuit

3.2 Back-EMF Based Position Estimation Method

The rotor position is obtained directly by measurement of the back-EMFs induced in the stator windings. In the basic operation of a BLDC motor, only two phases are energized at any instant with the other phase unexcited. Therefore, each of the motor terminal voltages contains the back-EMF information that can be used to derive the commutation instants [1], [19]. The zero-crossing method is employed to determine the switching sequence by detecting the instant where the back-EMF in the unexcited phase crosses zero. After detecting the commutation instant, the phase shifter is needed to get the correct commutation signal.

3.2.1 Zero-crossing detection

Generally, with Y-connected stator windings, the terminal voltages v_a , v_b and v_c can be derived as

$$v_a = v_{an} + v_n = Ri_a + L \frac{di_a}{dt} + e_a + v_n \quad (3-17)$$

$$v_b = v_{bn} + v_n = Ri_b + L \frac{di_b}{dt} + e_b + v_n \quad (3-18)$$

$$v_c = v_{cn} + v_n = Ri_c + L \frac{di_c}{dt} + e_c + v_n \quad (3-19)$$

where v_n is the neural voltage, v_{an} , v_{bn} and v_{cn} are the phase voltages, i_a , i_b and i_c represent the phase currents, and e_a , e_b and e_c are the phase back-EMFs generated in the three unexcited phase. From (3-17) to (3-19) can be derived as

$$v_a + v_b + v_c = (v_{an} + v_{bn} + v_{cn}) + 3v_n \quad (3-20)$$

Note that the current of the non-excited phase is zero if all the winding currents applied to the three phases are assumed to possess ideal rectangular shape without any disturbance. Hence, from (3-17) to (3-20), the back-EMF of the non-excited phase a can be derived as

$$e_a = v_a - v_n = v_a - \frac{1}{3}[(v_a + v_b + v_c) - e_a] \quad (3-21)$$

By simplifying (3-21), e_a can be estimated as follows

$$e_a = \frac{3}{2} \left[v_a - \frac{1}{3}(v_a + v_b + v_c) \right] \quad (3-22)$$

From (3-21) and (3-22), when e_a reaches to zero point, v_a can be estimated as

$$v_a = \frac{1}{3}(v_a + v_b + v_c) = v_n \quad (3-23)$$

The relationship between three terminal voltages and the waveform of back-EMF produced from (3-22) are shown in Fig.3.4. Therefore, the positions of the zero-crossing point could be detected from the back-EMF of phase a (e_a) when the electrical angles in the region of 0° - 60° and 180° - 240° as shown in Fig.3.4. In addition, e_{b-non} and e_{c-non} could be found in the same way.

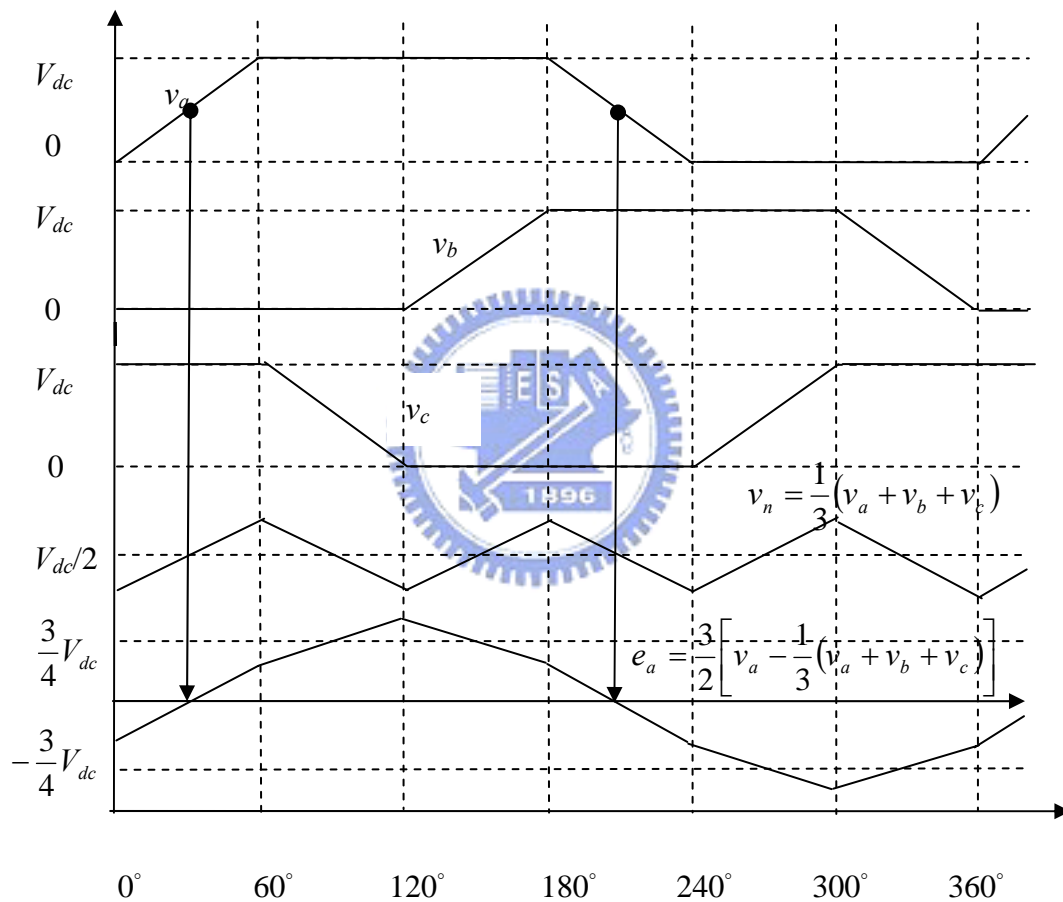


Fig.3.4 Ideal three terminal voltages and the waveform of back-EMF

After comparing the signals as presented in Fig.3.5, It could be found the relationship between the non-excited phase back-EMF (e_a) and Hall-effect signals (H_a). Thus, the zero-crossing points of the non-excited phases are required to be

delayed with 30 electrical degrees for generating the corresponding commutation signals instead of Hall-effect signals. The System schematic of sensorless BLDC motor drive is presented in Fig.3.6. Compared with System schematic of typical commutation control in Fig.2.5, the zero-crossing detection has replaced three Hall-effect sensors.

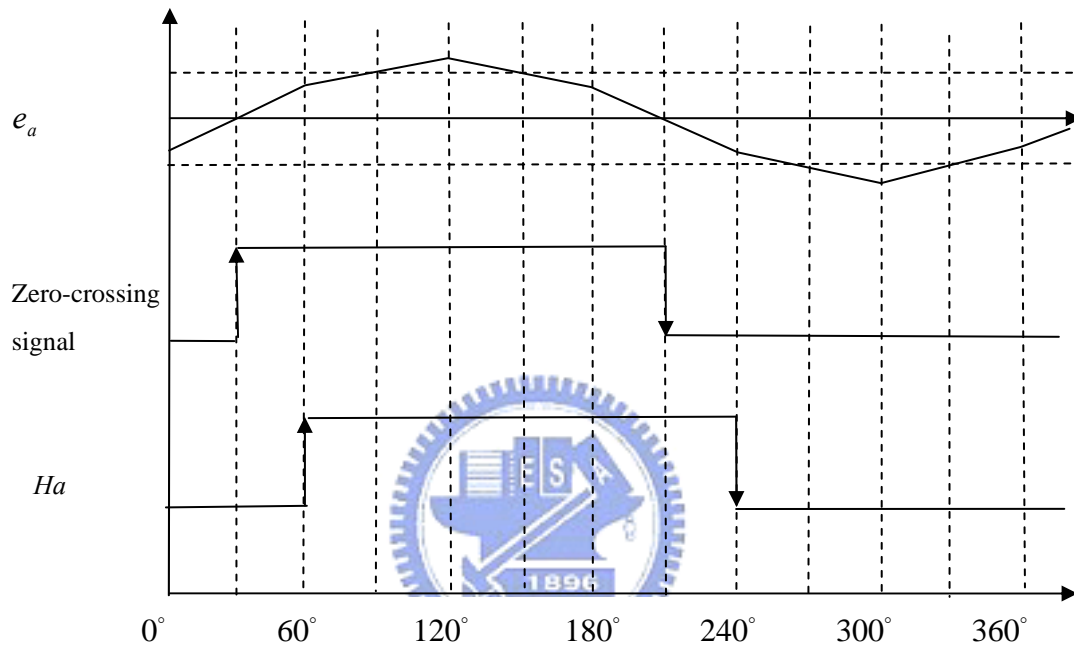


Fig.3.5 The relationship between the non-excited phase back-EMF and Hall-effect signals

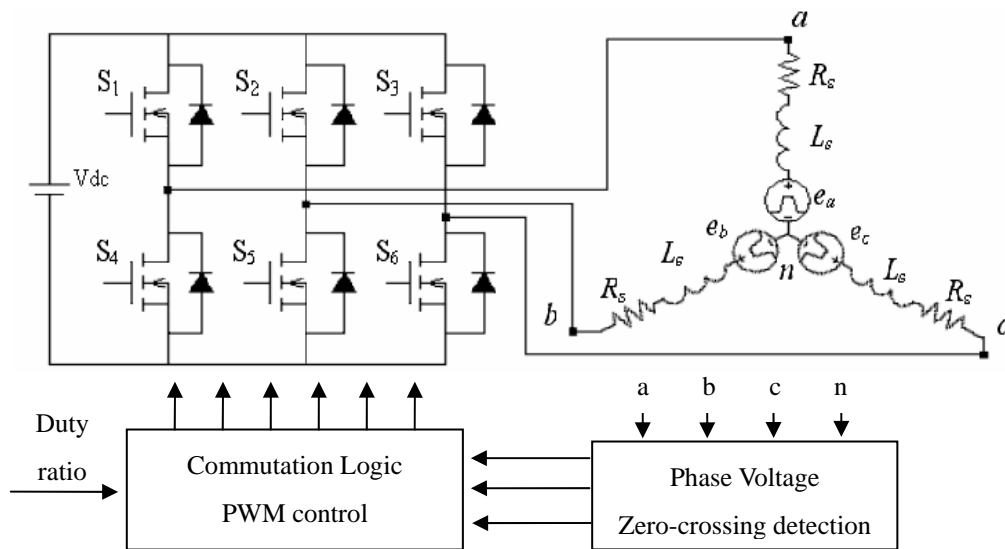


Fig.3.6 System schematic of sensorless BLDC motor drive

The method can be realized by using voltage sensors and low pass filters. However, the modulation noise is eliminated by using the low pass filters which is produced a phase delay varies with the frequency of the excited signal for the desired speed. Besides, since the back-EMF is zero at standstill and proportional to rotor speed, this method can not be used at zero speed and realizes difficultly at startup or very low situation.

3.2.2 Commutation phase shifter

After recognizing the zero-crossing signal of the estimated non-excited phase back-EMF, an additional 30° phase shift is required to perform correct commutation. Since the precision of the sensorless commutation control depends on the rotor speed, a

novel frequency-independent phase shifter (FIPS) [3] has been proposed. The algorithm of this phase shifter has been proven independent of input signal frequencies. However, the computation effort is quite large for real-time application; hence the digital simplified-type FIPS has been proposed in [1] as shown in Fig.3.7. Define the variable γ as the ratio of decreasing to increasing increments for the counters, $c_p(k)$ and $c_n(k)$, which are limited by a positive value L to avoid overflow condition at very low speed. Thus, $c_p(k)$ and $c_n(k)$ can be expressed as

$$c_p(k) = \min \left\{ \max \left[0, \sum_{m=k_p}^k \left(\frac{1 + \text{sgn}(x(m))}{2} - \frac{1 - \text{sgn}(x(m))}{2} \gamma \right) \right], L \right\} \quad (3-24)$$

$$c_n(k) = \min \left\{ \max \left[0, \sum_{m=k_n}^k \left(\frac{1 - \text{sgn}(x(m))}{2} - \frac{1 + \text{sgn}(x(m))}{2} \gamma \right) \right], L \right\} \quad (3-25)$$

with

$$\text{sgn}(x) = \begin{cases} 1, & \text{if } x \geq 0 \\ -1, & \text{if } x < 0 \end{cases} \quad (3-26)$$

where k_p is the largest k as $c_p(k) - c_p(k-1) < 0$, and k_n is the largest k as $c_n(k) - c_n(k-1) < 0$. Fig.3.8 illustrates the operational waveform of the proposed phase shifter. Assume that the input signal $x(k)$ in Fig.3.7 is the zero-crossing signal of the non-excited phase back-EMF as shown in Fig.3.5, and the output $y(k)$ is the corresponding commutation signal. Also, since commutations exist every 180° in Fig.3.5, γ can be represented as

$$\gamma = \frac{\pi}{\phi^*} \quad (3-27)$$

where ϕ^* is the desired degrees of the phase shift. Therefore, the decreasing increments are six-times larger than the increasing increments in order to make the phase shift $\phi^* = 30^\circ$. Besides, k_{zn} denotes the time when n th zero-crossing of input signal $x(k)$ occurs, and k_{cn} denotes the time when the commutation occurs. By definition, k_p is the largest k when $c_p(k) - c_p(k-1) < 0$, hence $k_p = k_{c1}$ when $k = k_{c1}$. As a result, the output signal $y(k)$ is changed from +1 to -1 at k_{c1} and the counter of $c_p(k)$ is disabled until next zero-crossing is triggered. On the other hand, k_n is the largest k when $c_n(k) - c_n(k-1) < 0$, hence $k_n = k_{c2}$ when $k = k_{c2}$. As a result, the output signal $y(k)$ is changed from -1 to +1 at k_{c2} and the counter of $c_n(k)$ is disabled until next zero-crossing is triggered. Therefore, the proposed digital phase shifter not only performs the frequency-independent characteristics, but also reduces computation effort.

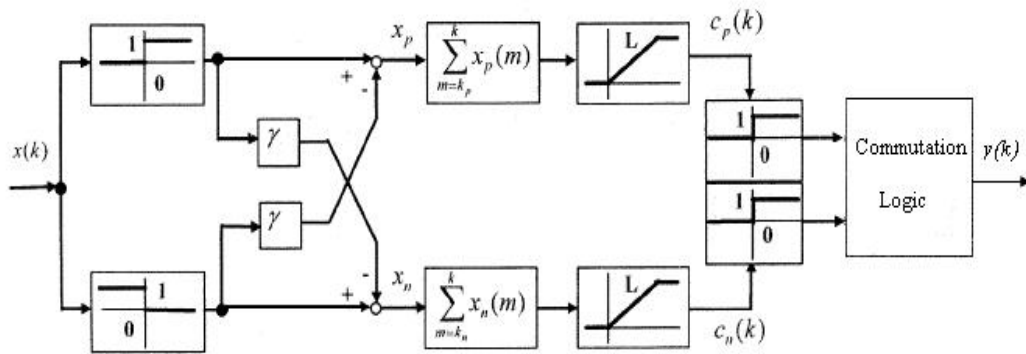


Fig.3.7 Block diagram of simplified-type FIPS

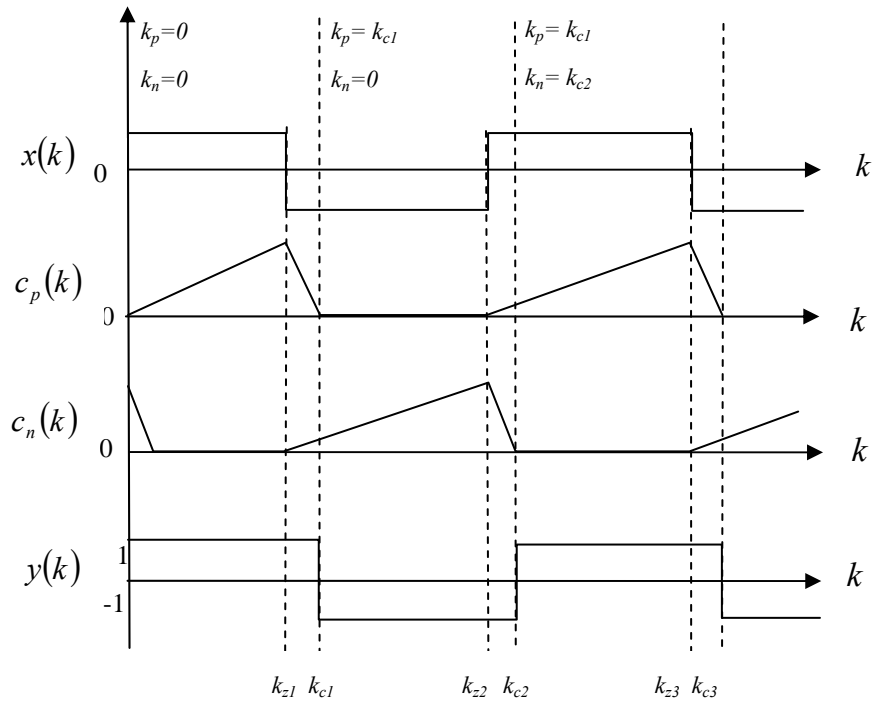


Fig.3.8 The operational waveform of the proposed phase shifter



Chapter 4

Start-up Strategy and Procedure for BLDC Motors

The start-up strategy is necessary since there is little or no back-EMF to sense when the motor is standstill or at a low speed. This chapter will introduce the start-up strategy in detail and the implementation of initial position detection and the start-up procedure for the BLDC motors.

4.1 Start-up Strategy

Since the back-EMF detection based position detection method cannot be used at start-up or low-speed, the additional start-up strategies are needed to solve these problems. Generally, the open-loop start-up algorithm can avoid this problem, in which strong current is flown to the output driver to force the rotor to move to the known rotor position [1], [20]. This open-loop algorithm has disadvantages of slow start and possibility of initial backward rotation [6]. Instead of open-loop start-up, inductive sense start-up algorithm is widely used in BLDC motor applications nowadays [10], [21]. In this section, these two methods will be introduced in detail.

4.1.1 Open-loop start-up method

The open-loop start-up method is accomplished by providing a rotating stator field which increases gradually in frequency. Once the rotor field begins to become

attracted to the stator field enough to overcome friction and inertia, the rotor begins to turn. However, the drawback of this method is the initial rotor movement is not predictable, which is inadequate for disk drives. Thus, the initial position detection is important in this method.

The motor starting procedure will be illustrated as follows: first, the rotor would be aligned from an unknown position to a certain position. Then set control signals to the driver circuit with a conducting sequence. If the initial position could be known accurately, this method could succeed in high probability.

4.1.2 Inductive sense start-up method

The main idea of this method is to utilize the fact that the inductance of the motor winding varies as the rotor position changes. The magnetic flux generated by the current in the stator winding can increase or decrease the flux density in the stator depending on the rotor position, leading to decrease or increase in induction due to the saturation of the stator. The relationship between inductance and flux linkage is shown as

$$\lambda_{phase} = \lambda_{PM} + Li \quad (4-1)$$

where λ_{phase} is the summation of the flux from the permanent magnet, λ_{PM} , and the flux from the current i . L is the inductance of the excited phase. Supply the current with positive or negative direction to the phase, as shown in Fig.4.1 [10]. The

variations of the inductance are derived as

$$L^+ = \frac{\lambda_{Phase} - \lambda_{PM}}{i^+} = \frac{\Delta\lambda^+}{i^+} \quad (4-2)$$

$$L^- = \frac{\lambda_{Phase} - \lambda_{PM}}{i^-} = \frac{\Delta\lambda^-}{i^-} \quad (4-3)$$

where L^+ and $\Delta\lambda^+$ are the inductance and flux linkage variation corresponding to the positive current i^+ is provided; L^- , $\Delta\lambda^-$ and i^- is opposite. It is obvious that L^+ is smaller than L^- due to $\Delta\lambda^+$ is smaller than $\Delta\lambda^-$. Consider the response of a phase voltage and current to the variation of the inductance. The phase voltage equation is expressed as

$$v_{an} = Ri + L \frac{di}{dt} + e_a \quad (4-4)$$

The back-EMF can be neglect when a motor is at standstill. Then, solve the differential equation; the phase current can be derived as

$$i = \frac{v_{an}}{R} \left(1 - e^{-\frac{R}{L}t} \right) \quad (4-5)$$

According to (4-5), the phase current has a different transient dependent on the inductance variation, which is determined by the relative position of the magnet and the direction of the current. It should be noted that i^+ has a faster response than i^- due to the time constant R/L^+ is larger than R/L^- , as shown in Fig.4.2 [10]. Therefore, the position information can be obtained by monitoring the phase current i^+ and i^- in an appropriate time interval.

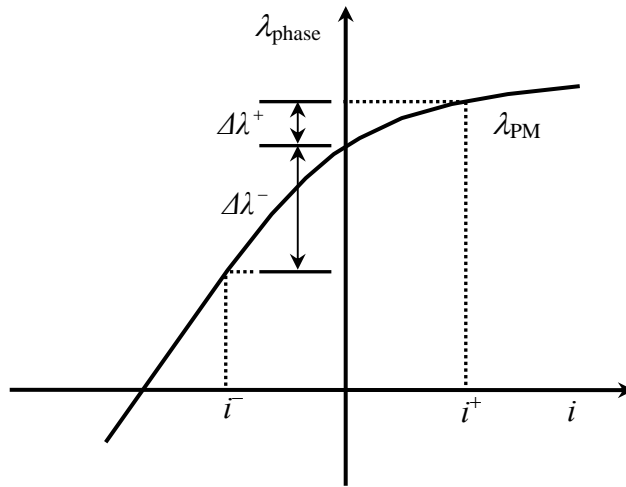


Fig.4.1 The flux linkage with positive or negative current

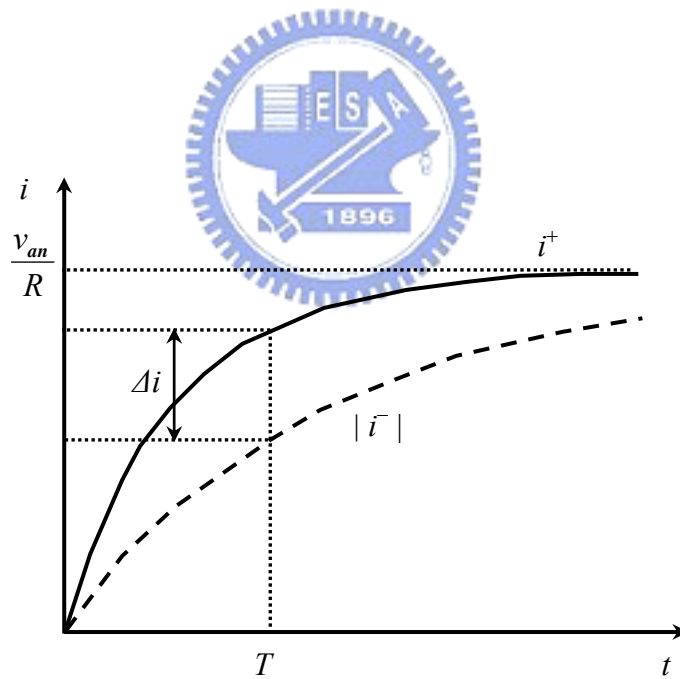


Fig.4.2 The responses of current with positive or negative direction

By applying positive and negative voltage pulses sequentially and measuring the difference in inductance, it can be determined which magnetic polarity the phase

winding is facing (Appendix A). Therefore, the initial position can be detected by the difference of the current pulse.

After identifying the initial position when a motor is at standstill, the correct phases winding on the stator are excited and the maximum electromagnetic torque is produced so that motor starts to rotate. Necessarily, the next commutation position should be detected for next excitation when the rotor rotates with 60 electrical degrees. However, the method proposed in previous section is not suitable while the rotor is rotating due to the time delay caused by the period of six voltage pulses and the negative direction torque produced by exciting incorrect segments. The start-up procedure proposed by G. H. Jang, J. H. Park and J. H. Chang [10] will be detailed illustrated in Appendix A.



However, the success of this algorithm strongly depends on how sensitive the inductance of the phase winding to the direction of the applied current at the given position. Therefore, the prototype motor which was unsuccessful with the inductive sense start-up algorithm will be investigated using finite element method (FEM) analysis for the identification of the root cause [13].

4.2 Start-up Procedure

In the section will verify the method introduced in Section 4.1 and represent the start-up procedure which will be used in the experiment for the BLDC motor since the start-up procedure is highly dependent on the characteristics of the motor.

4.2.1 Initial position detection

By using the initial position detection mentioned in Section 4.1, the relation of each segments of an electrical cycle will be implemented. As shown in Table 4.1, the three-phase motor has six segments of an electrical cycle, in which any two phases out of three currents. In order to verify the feasibility of this method, measured the current response with a delay 500 μ s. Besides, by using (4-5), the inductance is determined whenever a rotor moves the electrical angle of 12°. Therefore, Fig.4.3 could be plotted to show the relative rotor position with respect to the stator produces different response of the current i_l^+ and i_l^- . In addition, Fig.4.4 shows the variation of the difference responses di , which can provide information on the rotor position because the polarity of di changes every electrical angle of 60°, where $di_1=i_1^+ - i_1^-$, $di_2=i_2^+ - i_2^-$ and $di_3=i_3^+ - i_3^-$. The equilibrium positions (P₁~P₆), which means the relative magnitudes of the excitation currents in the two phases.

Table 4.1 Six segments of an electrical cycle

Segment	Symbol of current
\overline{AB}	i_1^+
\overline{BA}	i_1^-
\overline{CA}	i_2^+
\overline{AC}	i_2^-
\overline{BC}	i_3^+
\overline{CB}	i_3^-

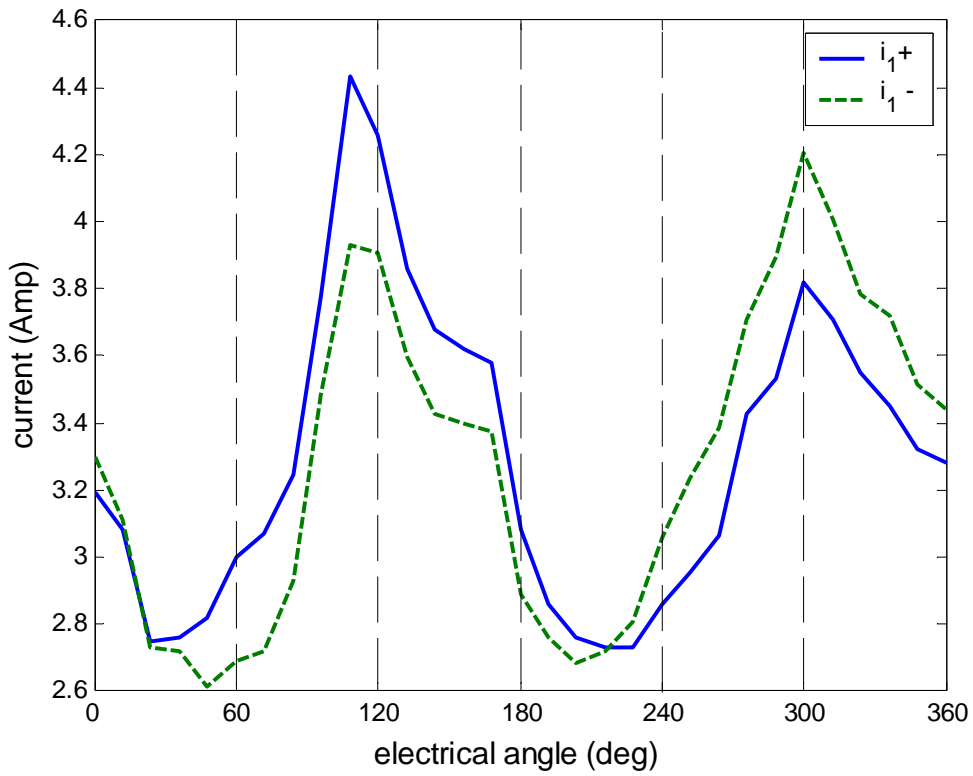


Fig.4.3 Current responses i_1^+ and i_1^- to the rotor position

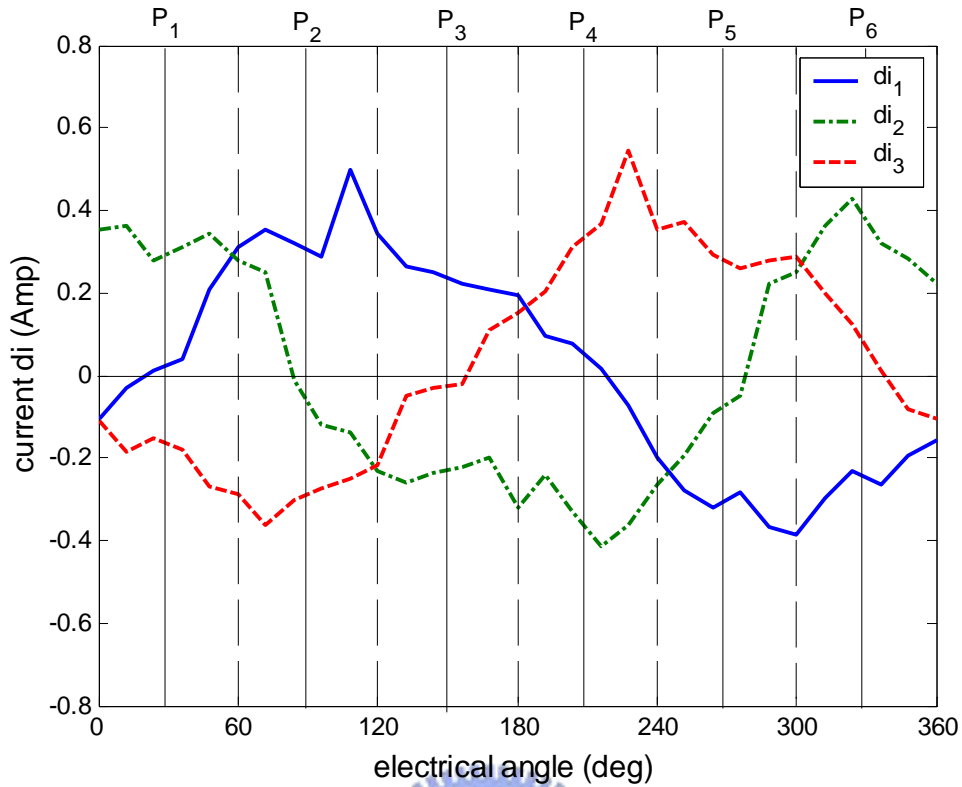


Fig.4.4 First difference of current responses to the rotor position

However, it is very difficult to identify the polarity of di near the magnetic equilibrium where a rotor tends to stop, because one of three di is zero in these positions. In these case, the polarity of second different of the current response, ddi , can be effectively used to identify the rotor position. Fig.4.5 shows the ddi for electrical period, where $ddi_1 = di_1 - di_2$, $ddi_2 = di_2 - di_3$, and $ddi_3 = di_3 - di_1$. Therefore, the polarity of ddi provides information on the rotor position near the equilibrium positions as shown in Table 4.2. Consequently, the stationary rotor position can be detected by ministering the polarity of di and ddi to energize the correct phases of the motor.

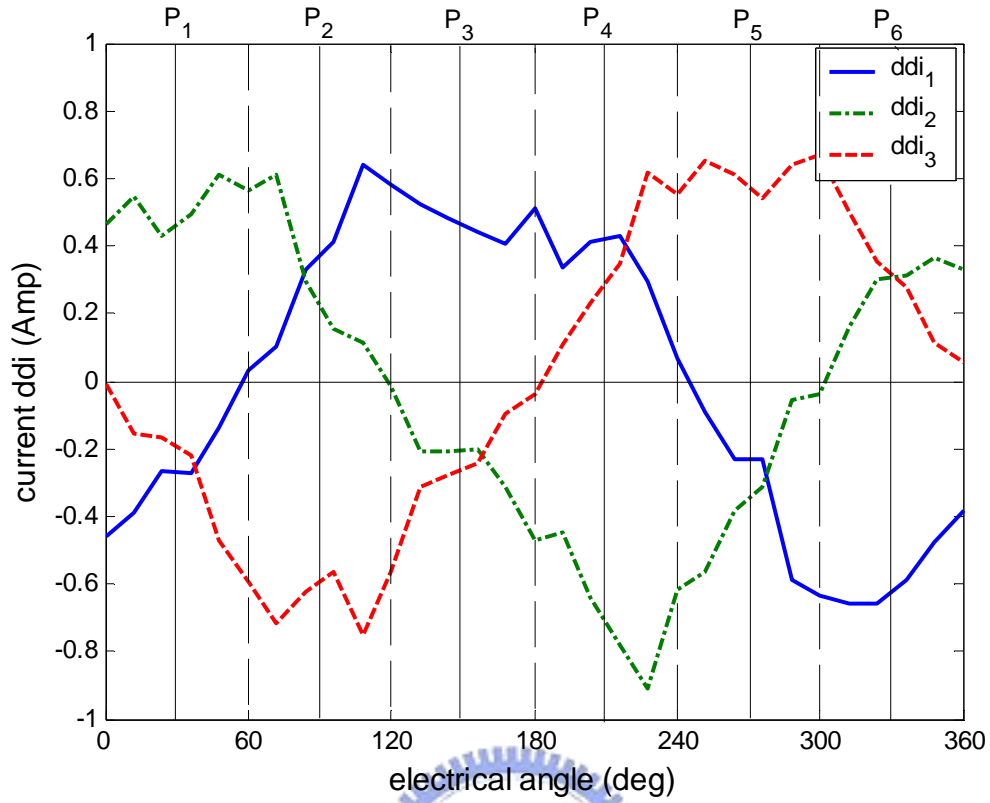


Fig.4.5 Second difference of current responses to the rotor position

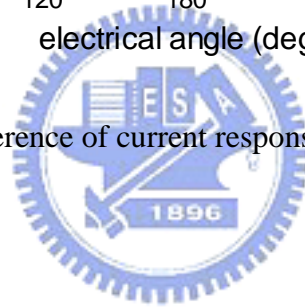


Table 4.2 Polarity of ddi on rotor position

Electrical position	ddi_1	ddi_2	ddi_3
$0^\circ \sim 60^\circ$	-	+	-
$60^\circ \sim 120^\circ$	+	+	-
$120^\circ \sim 180^\circ$	+	-	-
$180^\circ \sim 240^\circ$	+	-	+
$240^\circ \sim 300^\circ$	-	-	+
$300^\circ \sim 360^\circ$	-	+	+

4.2.2 Start-up from standstill

Consider the sampling rate is not high enough to implement the start-up algorithm proposed in [10] (see Appendix A.2), the open-loop method is used from standstill to the low angular velocity. After using the initial position detection to ensure the starting point, the next position should be right to avoid the initial backward rotation. However, the conventional open-loop method could not make the motor rotating smoothly from standstill since the torque input from software is too high. Therefore, the modified open-loop start-up method is proposed by using voltage pulse as shown in Fig.4.6.

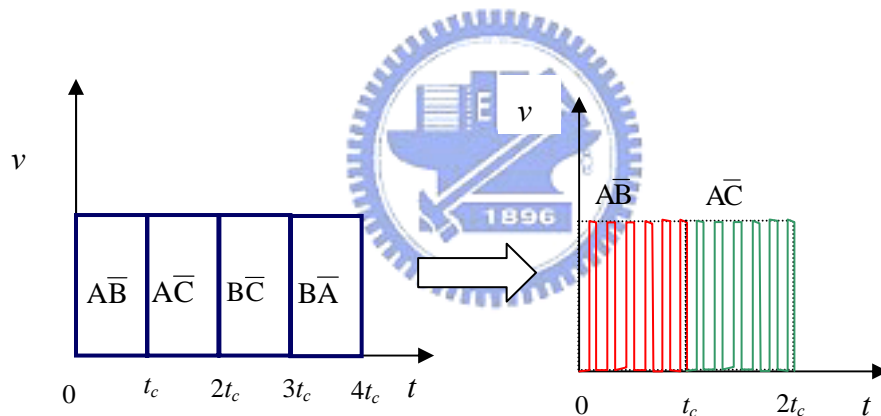


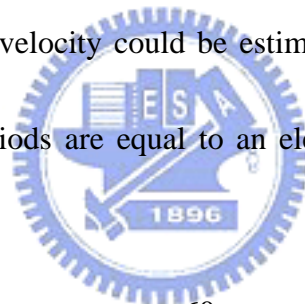
Fig.4.6 The modified open-loop start-up method

Define the six segments as sector 0~5 which are shown in Table 4.3. After detecting the initial sector, a set of position sequence will import the system and the motor will start to rotate in right direction. However, time delay is caused since the command instant is always faster than the motor arriving instant. Fig.4.7 shows the relation between the command signal and the circuit signal with initial sector 0. At

starting, the delay time is almost beyond a commutation time. After a period of time, the delay time will become less and approach to a constant. Then the system will switch to the commutation algorithm because there are enough back-EMFs to be detected.

As mentioned before, if there is no initial position detection, the initial backward will be incurred. For example, when the rotor initial position is in the sector 3 but the command is started in the sector 1, the rotor will rotate backward at the first commutation period as shown in Fig.4.8.

In addition, the angular velocity could be estimated by the commutation period because six commutation periods are equal to an electrical cycle. The mathematical equation is shown as



$$\hat{\omega} = \frac{60}{t_c \times 6 \times \frac{p}{2}} \quad (4-6)$$

where p is pole number and t_c is the commutation period. Since the velocity is changed by tuning the duty ratio, Table 4.4 will show the relation between the duty ratio and estimated angular velocity of the motor. By using the table, the open-loop start up method can be used from standstill to accelerate the velocity with decreasing time interval in the command signal.

Table 4.3 The definition of the position sector

Segment	Electrical position	Sector
\overline{CB}	$0^\circ \sim 60^\circ$	0
\overline{AB}	$60^\circ \sim 120^\circ$	1
\overline{AC}	$120^\circ \sim 180^\circ$	2
\overline{BC}	$180^\circ \sim 240^\circ$	3
\overline{BA}	$240^\circ \sim 300^\circ$	4
\overline{CA}	$300^\circ \sim 360^\circ$	5

Table 4.4 The relation between the duty ratio and estimated angular velocity

Duty ratio (%)	Angular velocity (rpm)	t_c (ms)
2	12.8997	9.6901
10	13.0691	9.5645
20	49.0097	3.5105
30	76.0586	1.6435
40	100.1600	1.2480
50	117.1875	1.0667
60	130.7909	0.9557
70	140.1903	0.8916
80	148.6549	0.8409
90	155.6351	0.8032
100	170.4790	0.7332

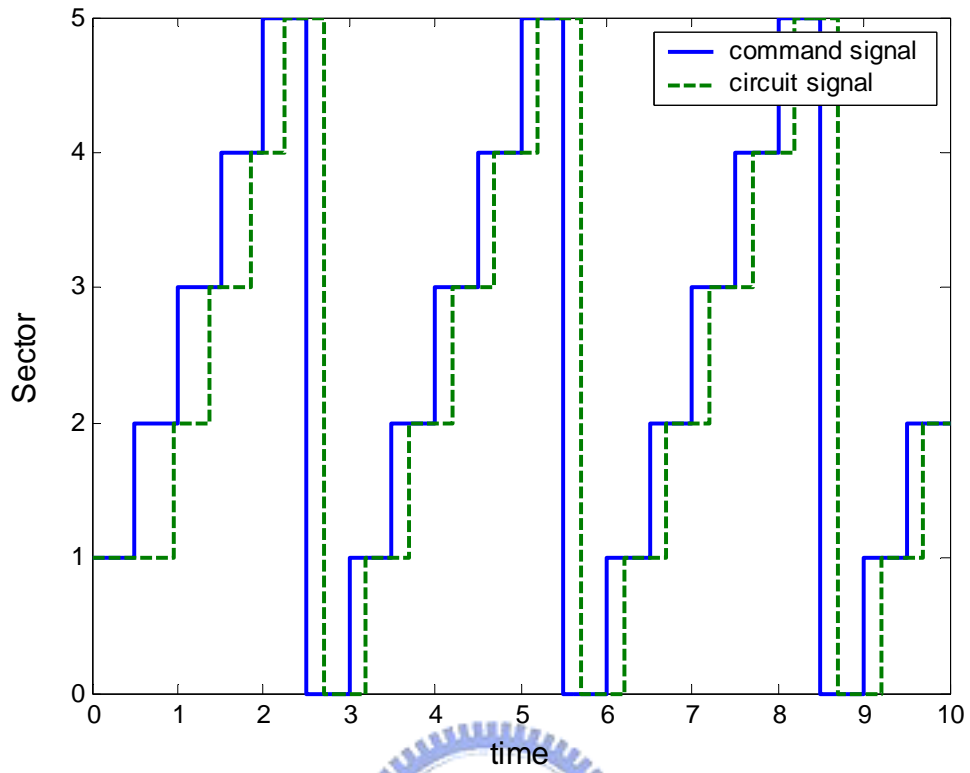


Fig.4.7 The relation between the command signal and the circuit signal

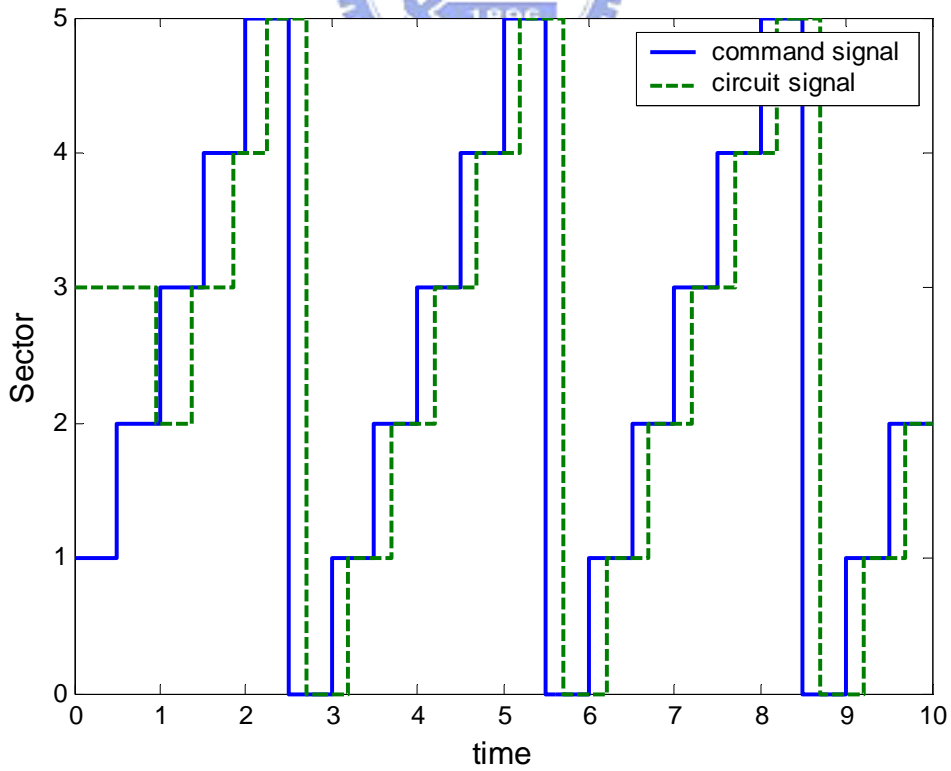


Fig.4.8 The relation signals without initial position detection

Chapter 5

Hardware Setup and Implementation of Sensorless Drivers

The theories and sensorless control strategies for the BLDC motor have been introduced in Chapter 3 and 4. In order to fulfill the control strategies, it is required to design sensorless drivers with good performance. Hence, this chapter will focus on the implementation of sensorless drivers. Besides, some experiments using PC-based drive system will be set up to verify the developed sensorless control strategies.

5.1 Experimental System Descriptions

The whole experimental system shown in Fig.5.1 consists of a BLDC motor, a driver circuit, AD/DA card, a PC-based control unit and a set of low-pass filters. The motor drivers will be discussed in Section 5.2.

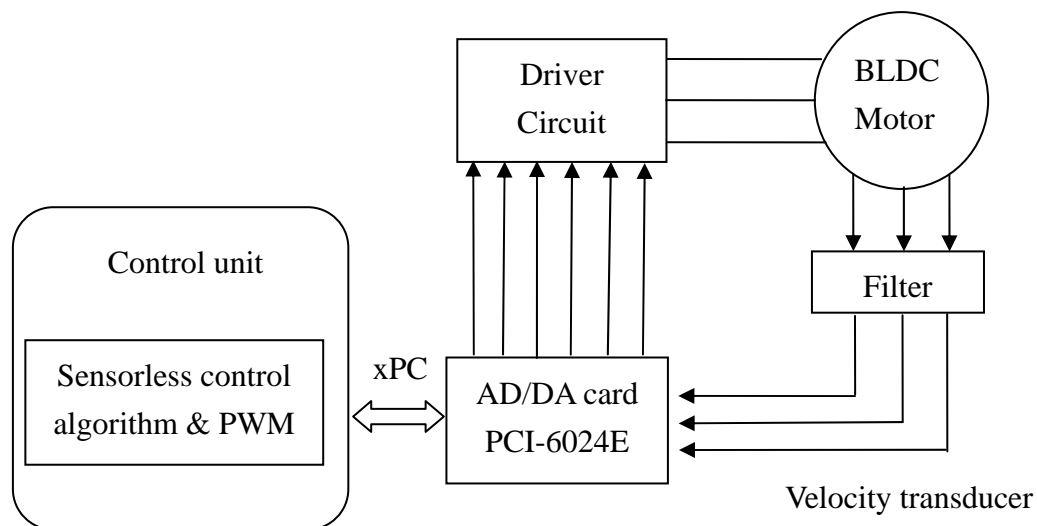


Fig.5.1 The complete hardware PC-based control system

A 3-phase BLDC axial-flux wheel motor, Crystalyte 4011, is used as the experimental plant, which is a low speed and high torque direct-drive motor with specifications listed in Table 5.1.

Table 5.1 The specification of the BLDC motor

Weight (kg)	6
Outer diameter of rotor (mm)	188
Outer diameter of stator (mm)	148
Length of PM (mm)	40
Pole numbers	16
Slot numbers	48
Coil numbers per phase	11
Phase resistance (Ω)	0.5
Phase inductance (mH)	0.001025
Operation voltage (volt)	36
Maximum unload speed (rpm)	177

In the second part, the AD/DA card, which is named PCI-6024E, is an I/O board with 16 single analog input (A/D) channels, 2 analog output (D/A) channels, 8 digital input and output lines. The maximum input sampling rate is 200kHz and the output sampling rate is 10kHz.

On the other hand, the control unit and AD/DA card are connected by the xPC target environment [12] which is shown in Fig.5.2, using two PC connected by

Ethernet line. One is a target PC; the other is a host PC. In addition, xPC target does not require DOS, Windows, Linux or any another operating system on the target PC. It is a kind of Real-Time environment with high sampling rate up to 20kHz. Furthermore, the PWM generator and sensorless control algorithm including the start-up algorithm and commutation control algorithm are realized in the host PC by software. In Section 5.3, the software design of these parts will be described in detail. Thus, the three inputs of the AD/DA card are the analog motor voltage, and six outputs are digital six-step drive signals.

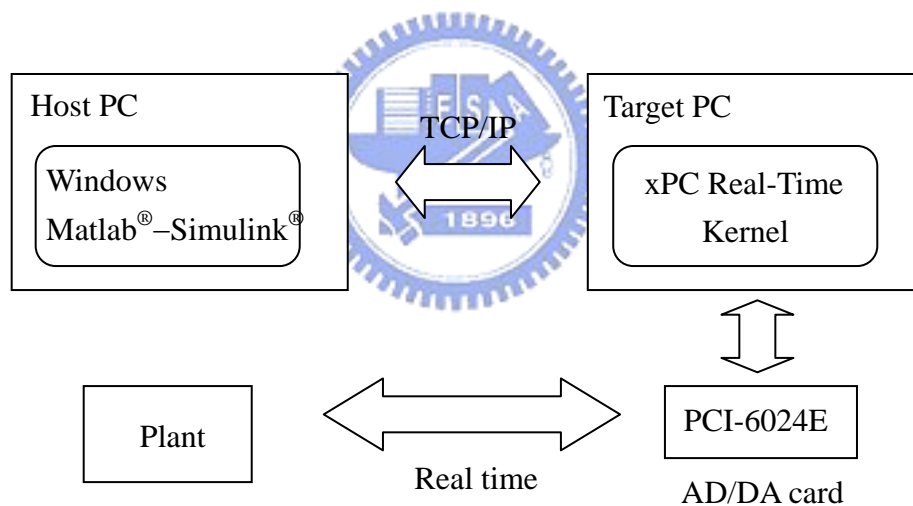


Fig.5.2 The block diagram of the xPC Target environment

Besides, after using pulse width modulation (PWM), the voltage signal will produce unwanted noises for detecting position in sensorless control algorithm. Therefore, a set of low pass-filters is needed to eliminate these inherent noises. Section 5.4 will analyze this part explicitly.

5.2 The Driver Circuit Unit

The use of the driver circuit unit is to realize the sensorless controller of a BLDC motor. The driver circuit unit consists of three parts: signal amplifier, half bridge driver unit and power MOSFET, whose block diagram is shown in Fig.5.3. There are six digital inputs required to control the current flow in the driver circuit unit, which are provided by the AD/DA card. The signal amplifier is needed due to the fact that the output high voltage of the AD/DA card is 5V [15] and the input of the half bridge driver unit is 15V [14].

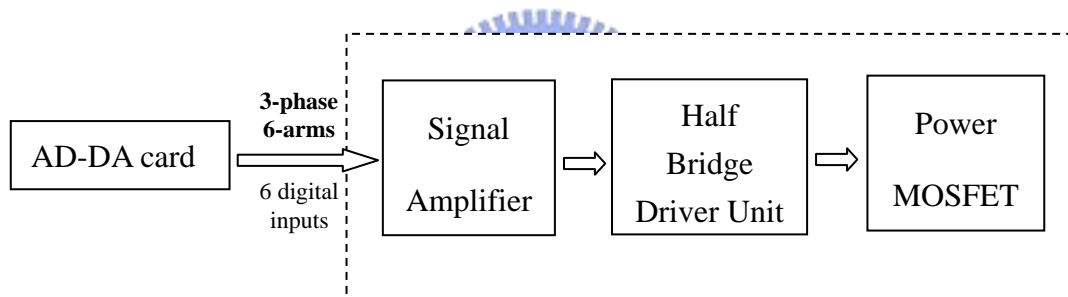


Fig.5.3 The block diagram of driver circuit unit

The half bridge driver unit is composed of three driver ICs, IR2113, which are high voltage, high speed power MOSFET drivers with independent high and low side reference channels. The floating channel at high side can be used to drive an N-channel power MOSFET which operates up to 600V. Besides, the gate drive supply ranges from 10 to 20V. The functional block diagram is shown in Fig.5.4. Each channel contains an under-voltage detect to ensure sufficient gate bias for the power MOSFET.

Another problem inherent to the half-bridge driver in the dead-time required between switching events. If there is not enough dead-time between turning one set of MOSFETs off and the next set on, a short circuit will appear across the dc bus. This creates large current spikes and will have a negative impact on circuit operation. To control the dead-time, the IR2113 has Schmitt trigger inputs. This allows the use of a simple RC circuit to control the time delay between receiving a gate signal input and the chip actually seeing that input.

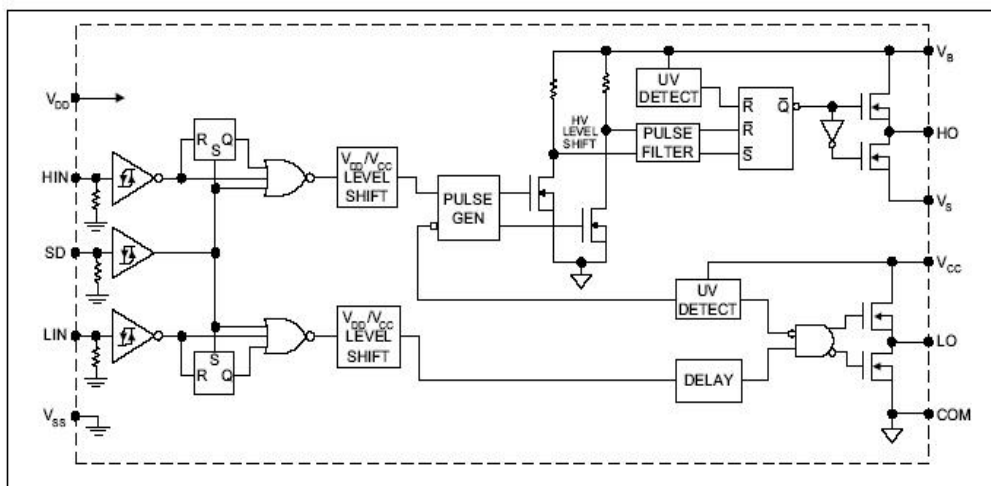


Fig 5.4 The functional block diagram of IR2113 [14]

Fig.5.5 shows the typical connection of IR2113 to power MOSFET. Each phase of motor is driven by two power MOSFETs (IRF640N) [16]. One of the most critical issues in a high power motor driver is to construct a circuitry that will be able to drive the high side power MOSFET. Since the source of this device is connected to one end of the phase coil, the voltage level of this node is floating due to

the induced voltage on the phase coil. So, the gate voltage of the high side power MOSFET must be set accordingly to provide proper operation of this device.

In Fig.5.5, the bootstrap principle is applied to the floating channel. First, suppose that the bootstrap capacitor C_1 has been charged enough voltage ($V_{c1} \approx V_{cc}$) by an external source V_{cc} over a bootstrap diode during the period when S_1 is OFF. When HIN is high, M1 turns on and M2 turns off, and then V_{c1} will charge the capacitor between the drain and source of S_1 through M1, i.e., V_{c1} works as a voltage source at this time. When HIN is low, M1 turns off and M2 turns on, and then the charge in S_1 will be released rapidly through R1 and M1. Finally, S_1 is OFF, and LIN changes to high voltage after passing the dead-time.

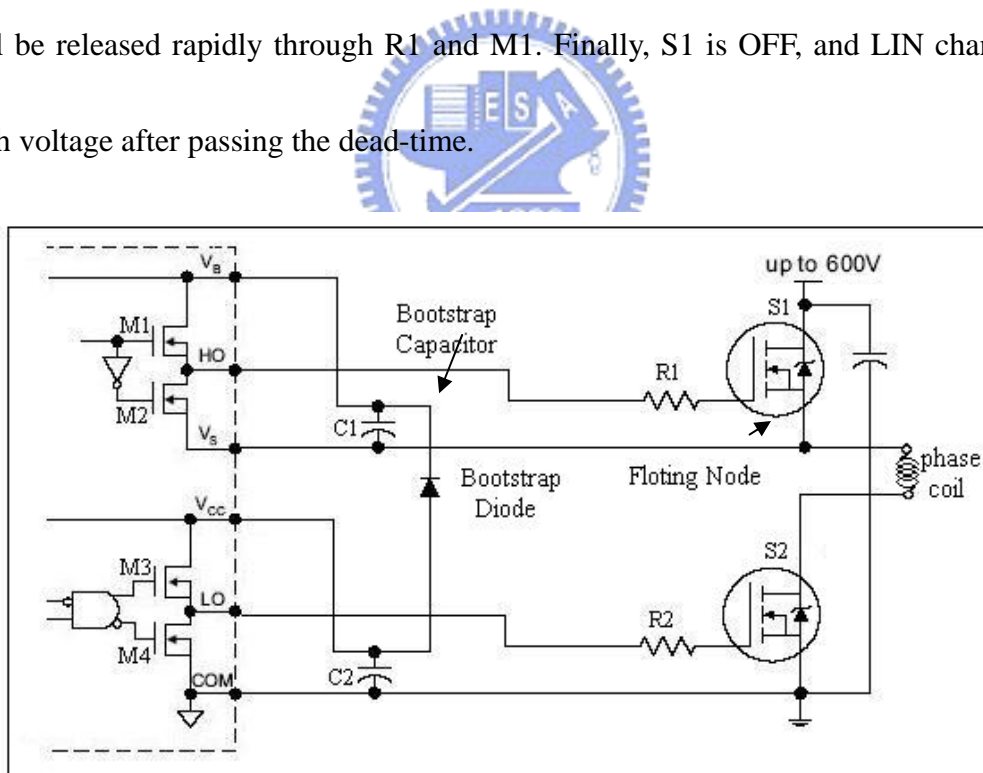


Fig.5.5 The typical connection of IR2113 to power MOSFET

The total driver circuit will be shown in Fig.5.6 and the photo of motor drive circuit will be displayed in Fig.5.7. There are six inputs connected to AD/DA card and

three outputs connected to the three phase of the motor.

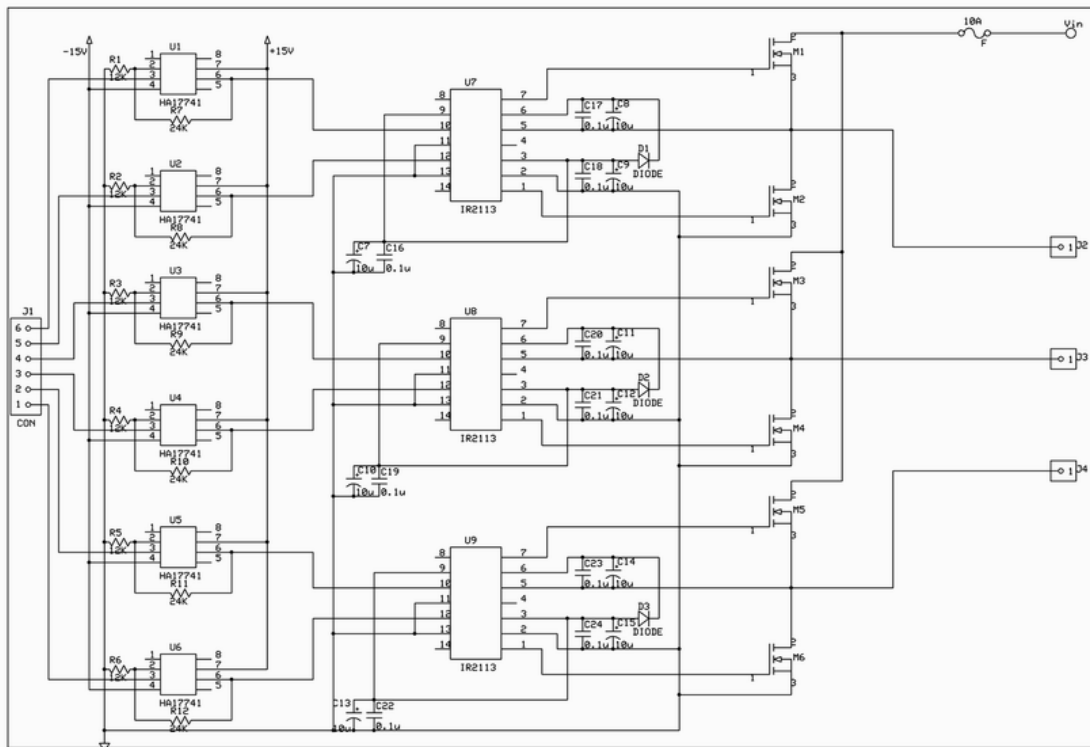


Fig.5.6 The three phase motor driver circuit

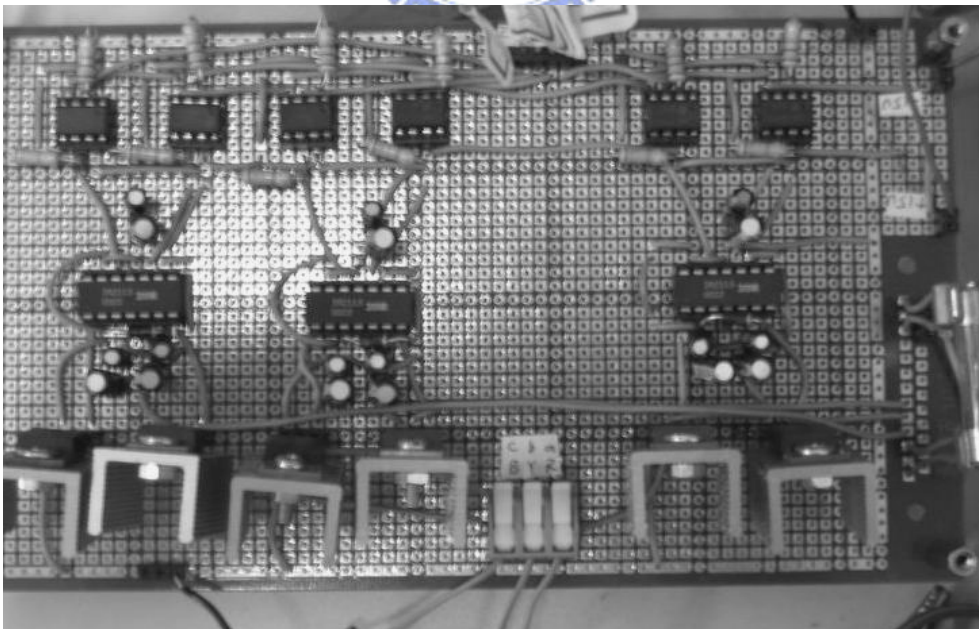


Fig.5.7 The motor driver circuit

5.3 The Sensorless Control Unit

The sensorless control unit is fulfilled by the software package simulink[®], including control algorithm, 3-to-6 signal transformation and pulse width modulation (PWM). The block diagram of the sensorless control unit is shown in Fig.5.8.

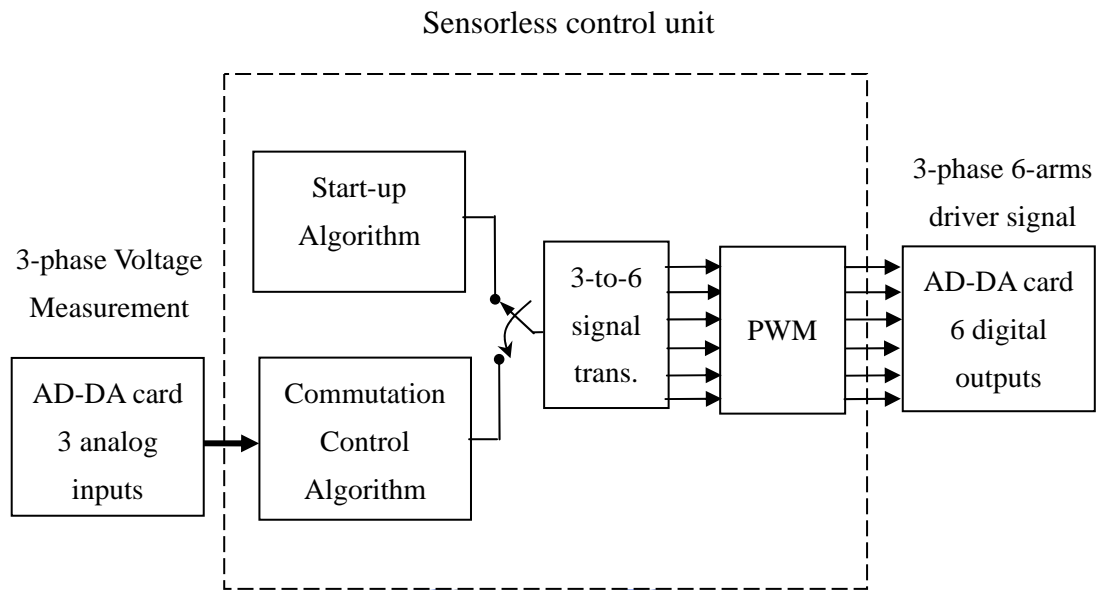


Fig.5.8 The block diagram of sensorless control unit

The control algorithm block is to realize the start-up method mentioned in Section 4.2 and sensorless commutation control method given as (3-17) to (3-26) with inputs of the motor's phase voltages and outputs of the three-phase commutation signals. Then the 3-to-6 signal transformation block fulfills the phase commutation sequence as shown in Table 5.2, where the six outputs (a_{up} , a_{down} , b_{up} , b_{down} , c_{up} , and c_{down}) are determined by the inputs of the three-phase commutation signals (S_a , S_b , and S_c). These

six outputs are used as the switches to turn on or turn off the power MOSFET in driver circuit unit. Fig.5.9 shows the results of the trapezoidal back-EMFs and the phase current generated by the switching.

Table 5.2 the phase commutation sequence

segment	Commutation signal			MOSFET switch					
	S_a	S_b	S_c	a_{up}	a_{down}	b_{up}	b_{down}	c_{up}	c_{down}
\overline{CB}	0	0	1	0	0	0	1	1	0
\overline{AB}	1	0	1	1	0	0	1	0	0
\overline{AC}	1	0	0	1	0	0	0	0	1
\overline{BC}	1	1	0	0	0	1	0	0	1
\overline{BA}	0	1	0	0	1	1	0	0	0
\overline{CA}	0	1	1	0	1	0	0	1	0

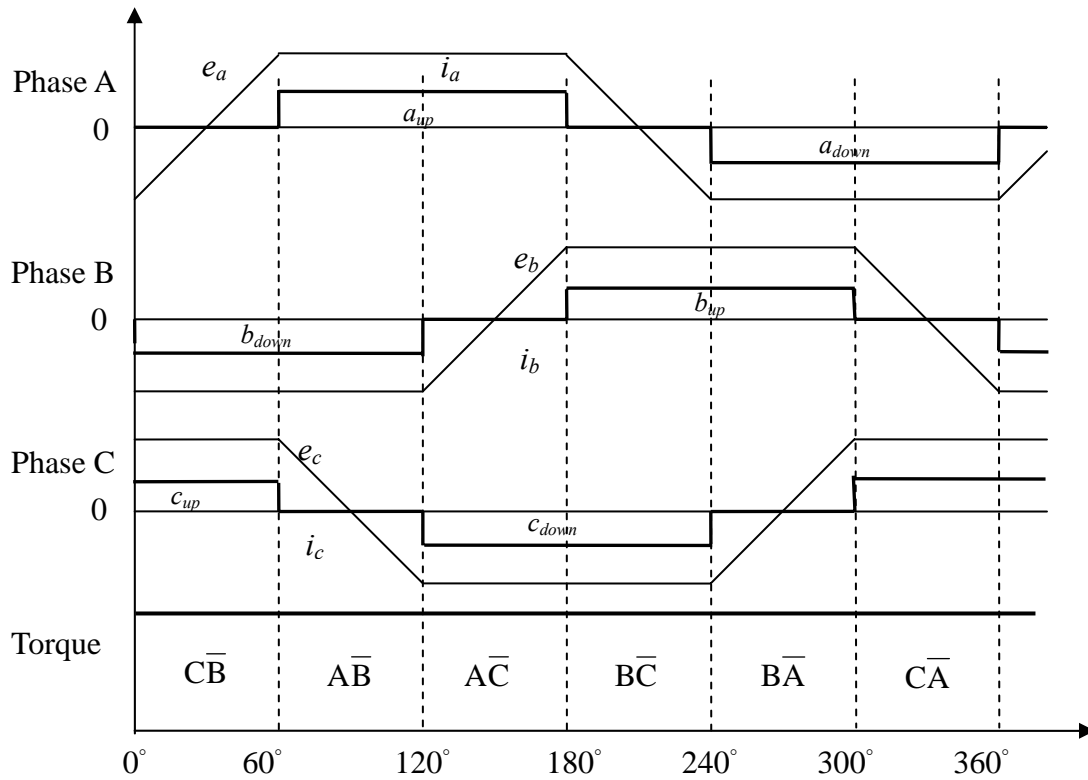


Fig.5.9 The ideal trapezoidal back-EMFs and torque production in a Y-connected three phase BLDC motor

As usual, in a PWM signal, the frequency of the waveform is a constant while the duty cycle varies (from 0% to 100%) according to the amplitude of the original signal. In addition, the PWM is used to control the power applied to the motor. It can control the voltage on the motor with a fixed PWM duty cycle. The PWM usually can be applied in three ways: on the high side, on the low side, and on both sides [17]. Among them, PWM on the high side is more useful since the back-EMF can be read.

For example, in Fig.5.10(a), when the related switches T2 and T3 are ON, the current passes through the two switches and two motor windings. The potential on the point M is $HV/2$ and the back-EMF can not be read because the voltage is too high.

When the high side is switched OFF in Fig.5.10(b), the current inside the motor continues to flow in the same direction. While the switch is off, the current can only use the diode D5. Assume that V_{on} is the turn ON voltage of the switch, and V_f is the forward voltage of a diode. In this case, the potential in A is the V_{on} of switch T3, the potential in B is $-V_f$ of D5, and the potential in M is $(V_{on}-V_f)/2$. It is close to zero because in most cases $V_{on}=V_f$. Thus the complete back-EMF referred to the ground terminal on the phase C can be read by voltage measurement.

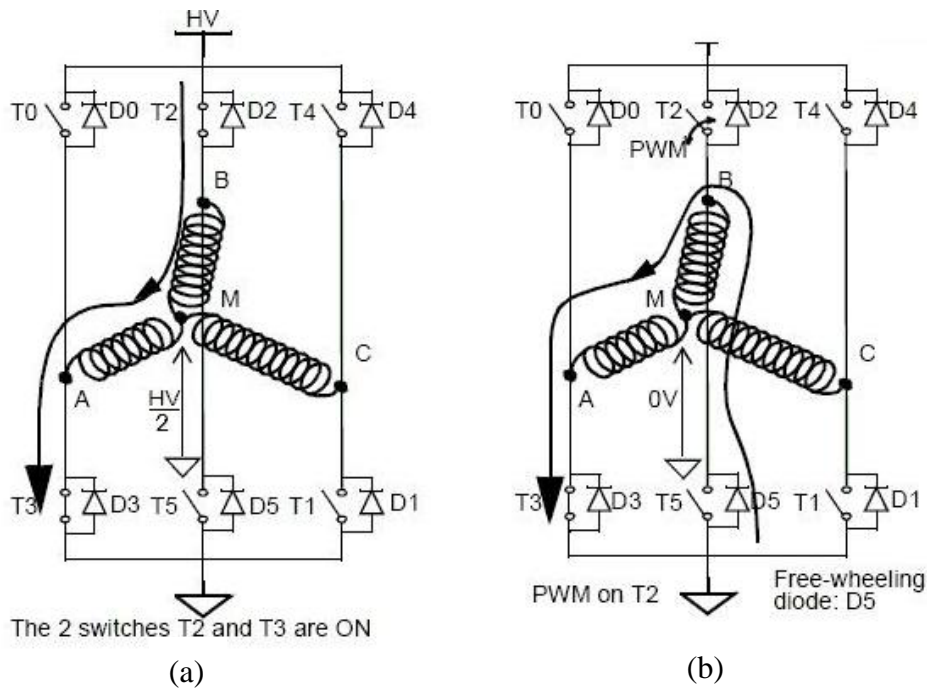


Fig.5.10 PWM on the high side: (a) current during ON time, (b) Current during OFF time

5.4 Filter Circuit Unit

The purpose of the low-pass filter is to eliminate the noise generated by the PWM.

A Fourier analysis of a typical PWM signal is shown in Fig. 5.11. There is a strong peak at frequency $F_n = 1/T$, and other strong harmonics also exist at $F = K/T$, where K is an integer. These peaks are unwanted noises and should be eliminated by low-pass filter.

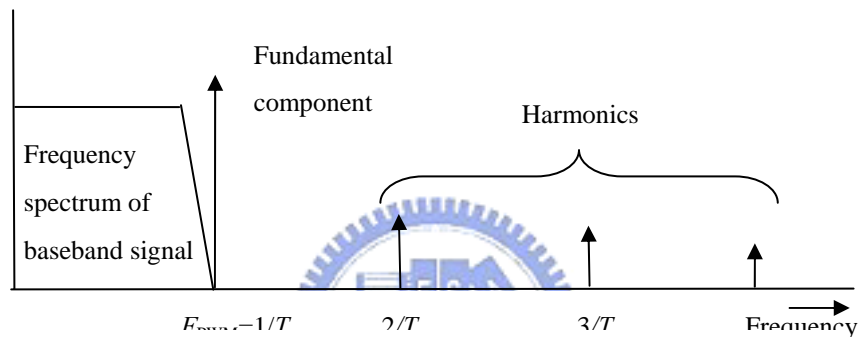


Fig.5.11 Frequency spectrum in a PWM signal

Therefore, the band-width of the desired signal should be smaller than the fundamental component at $F_{PWM} = 1/T$. As shown in Fig.5.12, chosen the band-width frequency F_{BW} to satisfy $F_{BW} \ll F_{PWM}$ such that

$$F_{PWM} = K \cdot F_{BW} \quad (5-1)$$

where K is a constant and $K \gg 1$. The value of K should dependent upon the number dB such that the inherent fundamental noise component of PWM will be rejected.

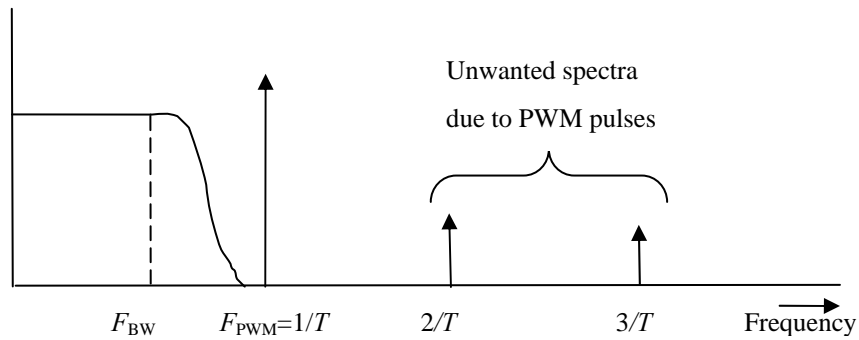


Fig.5.12 External low-pass filter

In the experiment, the frequency of PWM is 1KHz, so it is required to design a simple RC low-pass filter to obtain an analog voltage output. To analyze the value of K in (5-1), the bode plot of the RC low-pass filter will be shown in Fig.5.13. First, choose $K=2$, thus F_{BW} of the low-pass filter will equal to 500Hz. So, the fundamental noise peak will be filtered at 1KHz. In this figure, the main peak of PWM signal is cut-off about -7dB. Generally, this rejection of -7dB will not suffice. When $K=4$, the main peak of PWM signal is cut-off about -12.3dB. However, the phase delay is more than the first case. Since it is a real-time feedback control system, the phase delay would affect the accuracy in the experiment. Thus, when K is large, the rejection of the main peak would be better but the phase delay would be more.

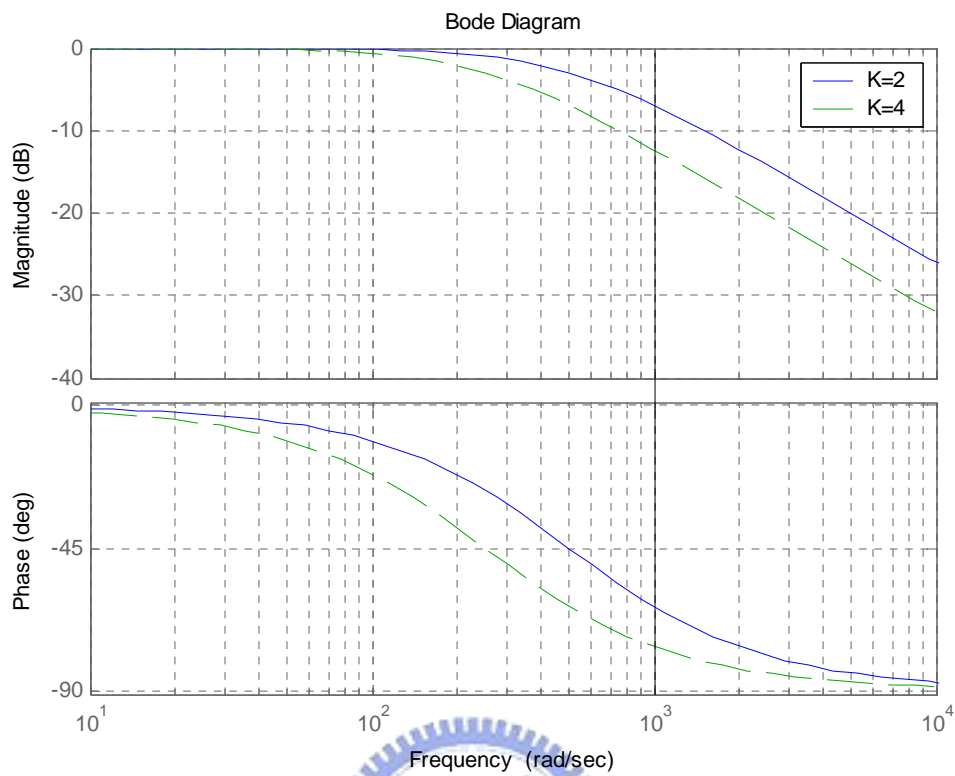


Fig.5.13 Bode plot of the external low-pass filter

Design a low-pass filter to suffice $K=4$, the band-width frequency is equal to 250Hz. Using relation $RC = 1/2\pi f$, R is chosen as $6.4K\Omega$ and C is chosen as $0.1 \mu F$.

The design circuit is shown in Fig.5.14. The voltage follower is used as a buffer between devices to avoid loading errors.

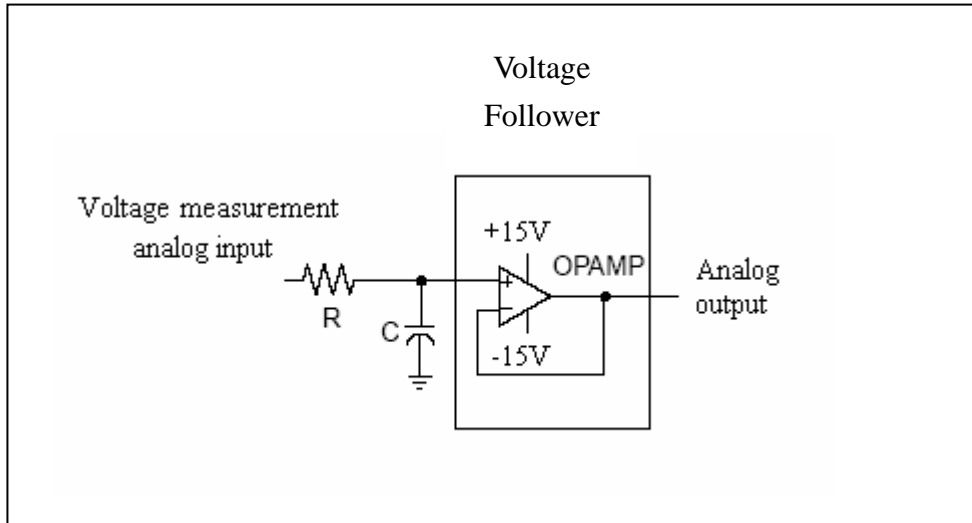


Fig.5.14 The external low-pass filter circuit



Chapter 6

Experimental results and analysis

In order to verify the effectiveness of the sensorless commutation control strategy and the start-up method, the experimental results will be shown in this chapter. According to the measurement result of the phase voltage and current, the information of the back-EMF and commutation signals will be produced by the sensorless strategies mentioned in Chapter 3.

6.1 Experimental results of the Commutation Control

The sensorless control method is realized in software. Fig.6.1 and Fig.6.2 will be show the block diagram in Matlab[®]-Simulink[®]. Fig.6.1 is the overall sensorless control algorithm with three terminal voltage inputs and three estimated Hall-sensor output produced from the algorithm. Fig.6.2 is the block diagram frequency independent phase shifter (FIPS).

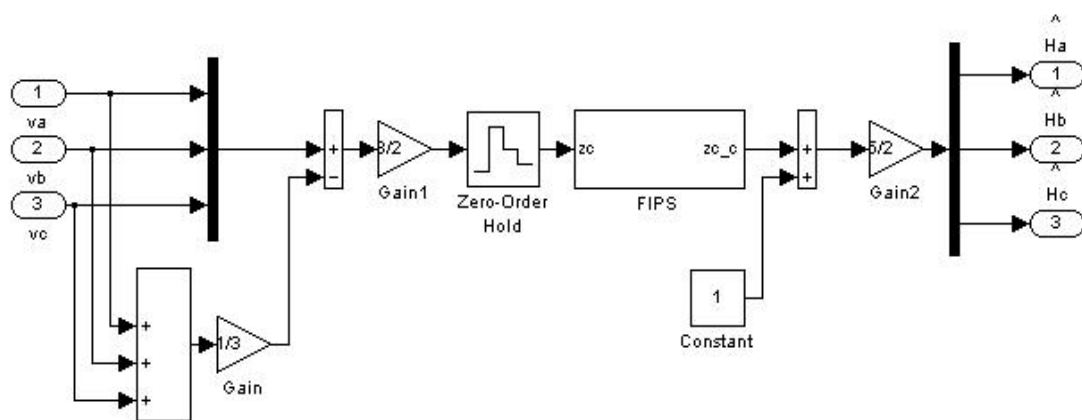


Fig.6.1 The block diagram of overall sensorless control algorithm

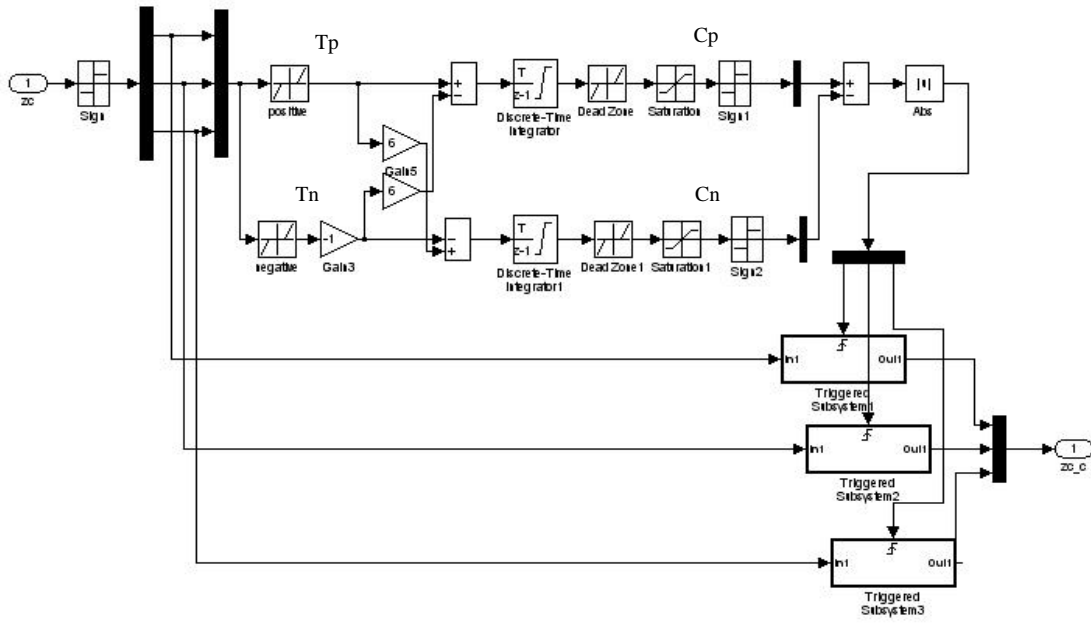


Fig.6.2 The block diagram of frequency independent phase shifter (FIPS)

The three terminal voltages measured directly from the BLDC motor are shown in Fig.6.3 and 6.4. To analyze the experimental results at high angular velocity (about 170.5 rpm) and low angular velocity (about 49.7 rpm), it could be found that the zero crossing point in a low angular velocity is hard to detect. Therefore, an additional low-pass filter is needed before the voltages are transferred into the PC. By analyzing the frequency spectrum as shown in Fig.6.5, a set of low-pass filter could be designed to eliminate the unwanted noises as described in Section 4.4. After using the low-pass filter, the frequency spectrum of terminal voltage is shown in Fig.6.6. Fig.6.7 shows the terminal voltage in a low angular velocity after using the low-pass filter.

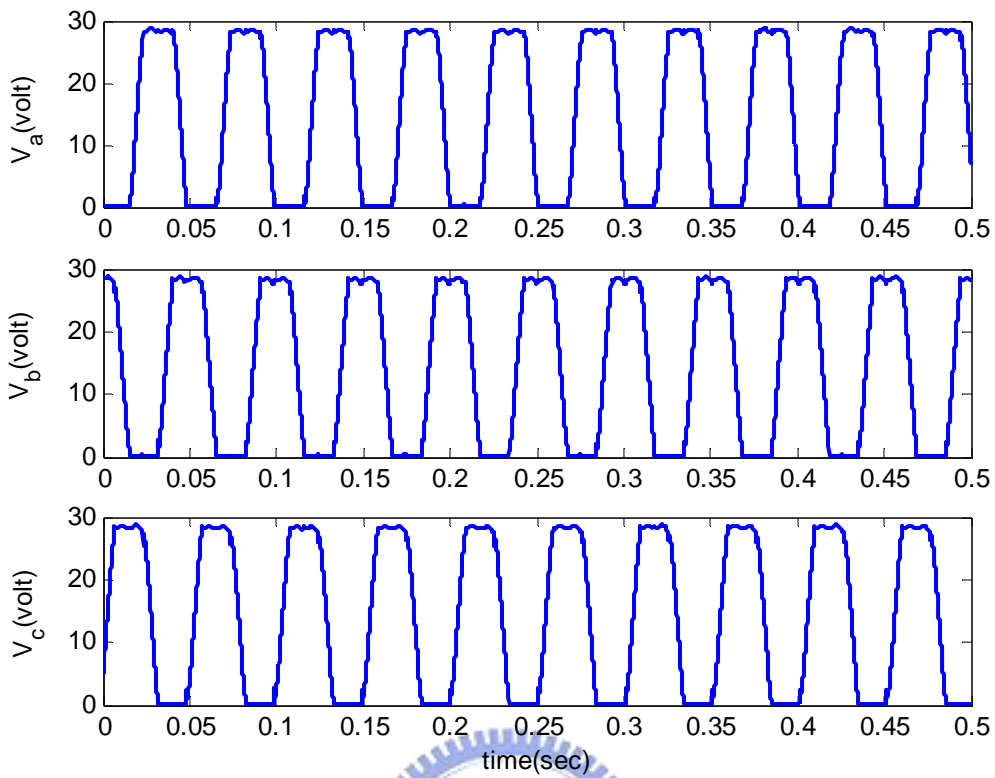


Fig.6.3 Terminal voltage at high angular velocity

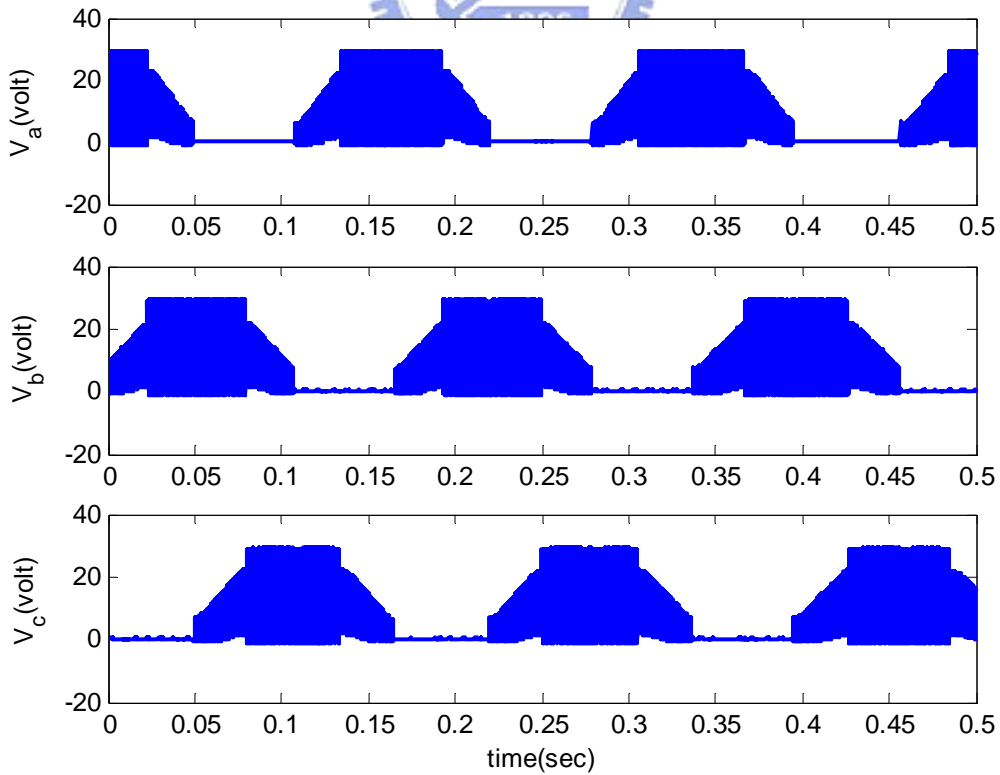


Fig.6.4 Terminal voltage at low angular velocity

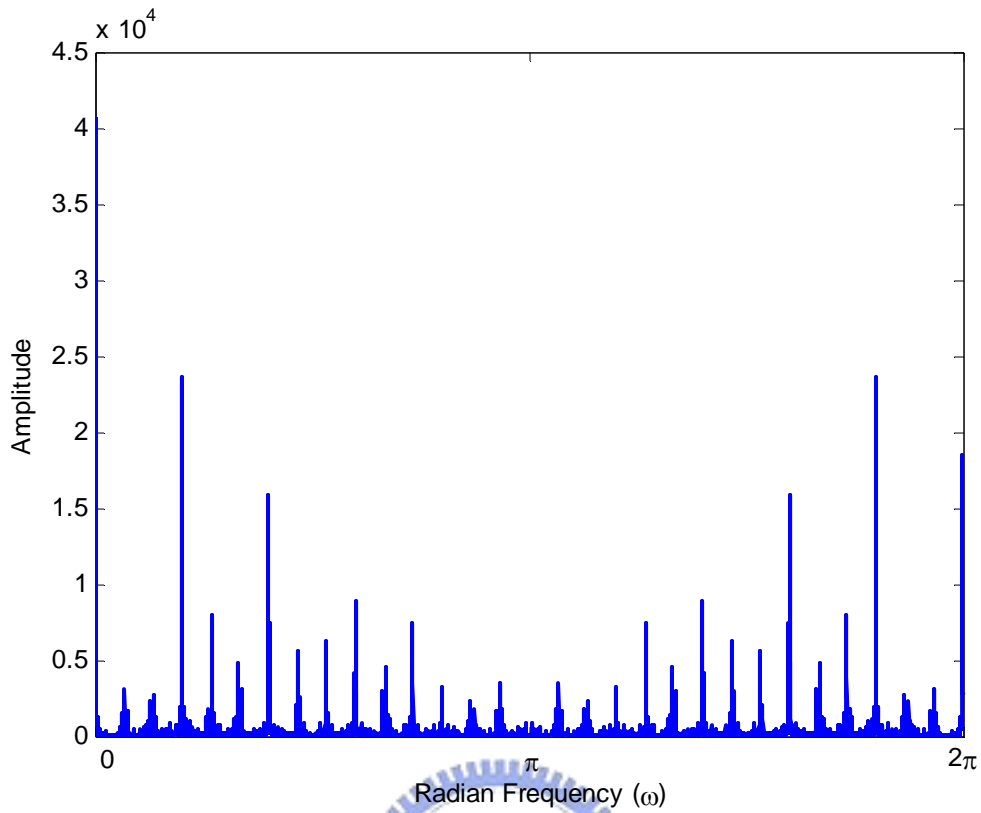


Fig.6.5 Frequency spectrum of terminal voltage at low angular velocity

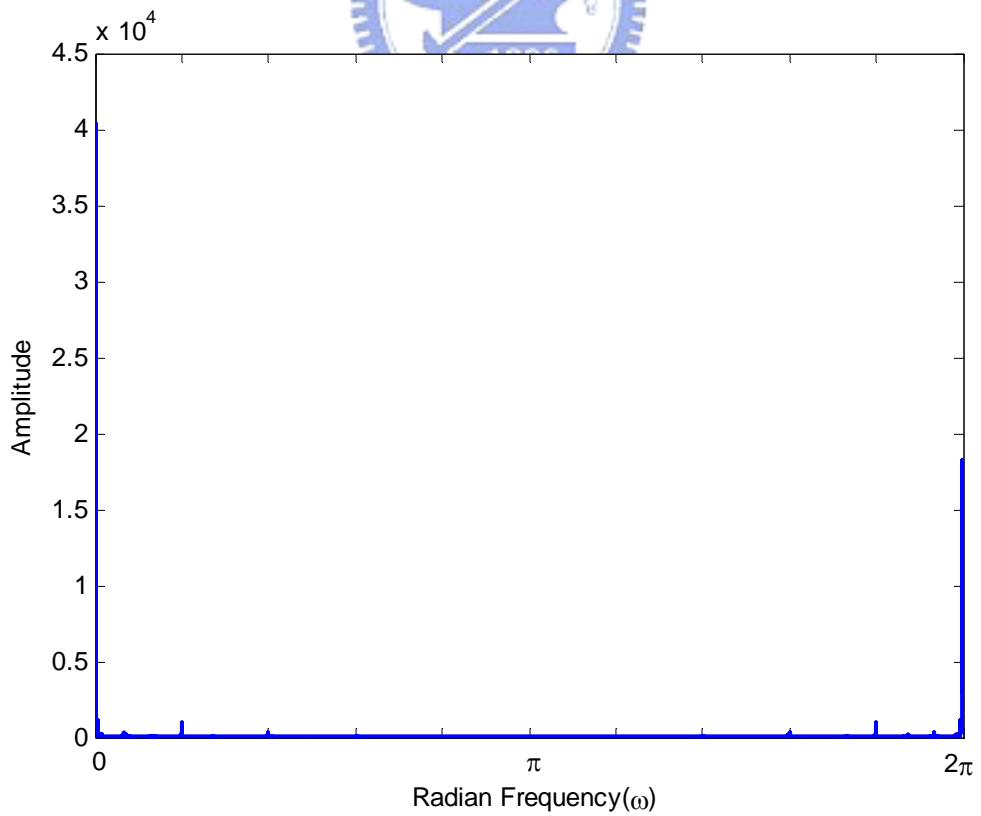


Fig.6.6 Frequency spectrum of terminal voltage after using the low-pass filter

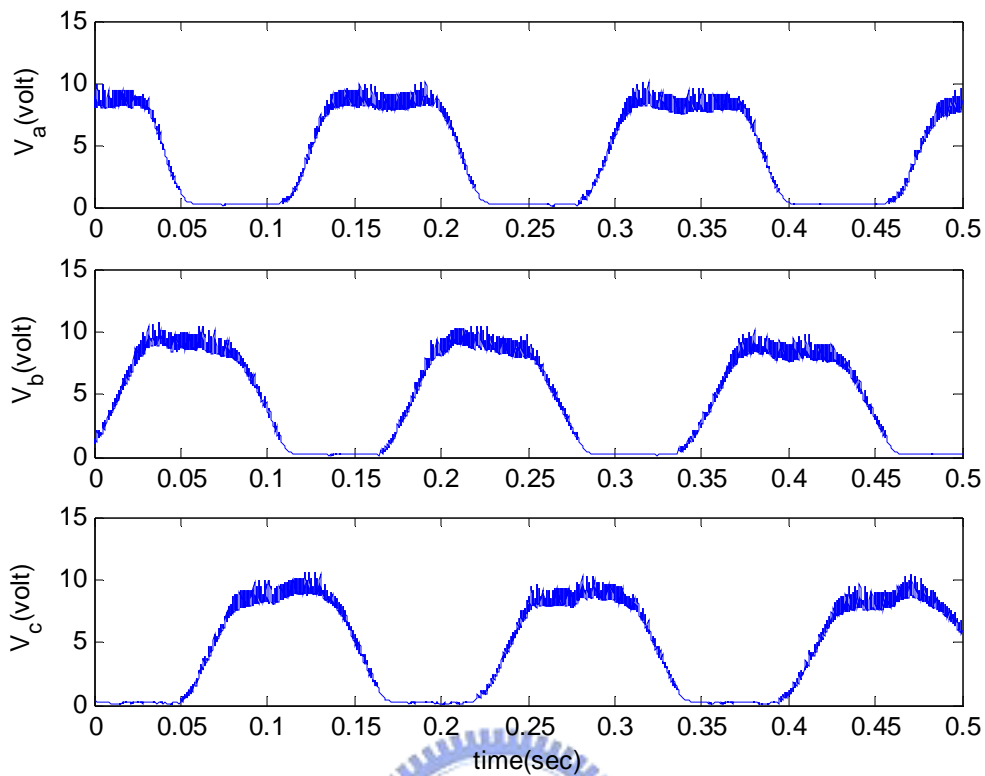
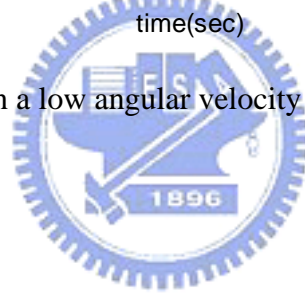


Fig.6.7 Terminal voltage in a low angular velocity after using the low-pass filter



After using the low-pass filter, the zero-crossing points are easier to detect for sensorless algorithm. Then the experimental results of the sensorless control in high angular velocity will be shown in Fig.6.8 and Fig.6.9; and a low angular velocity will be shown in Fig.6.10 and Fig.6.11. Finally, the comparisons between the sensorless produced signals and conventional Hall-effect signals will be shown in Fig.6.12 and Fig.6.13.

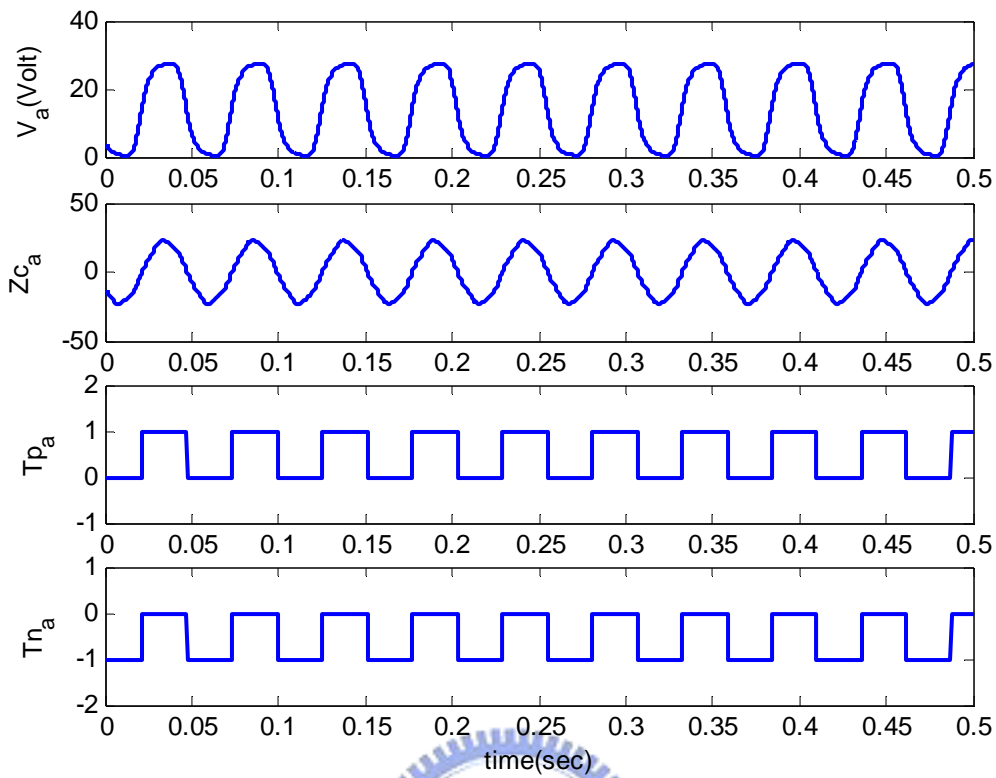


Fig.6.8 Sensorless control performance at high angular velocity (I)

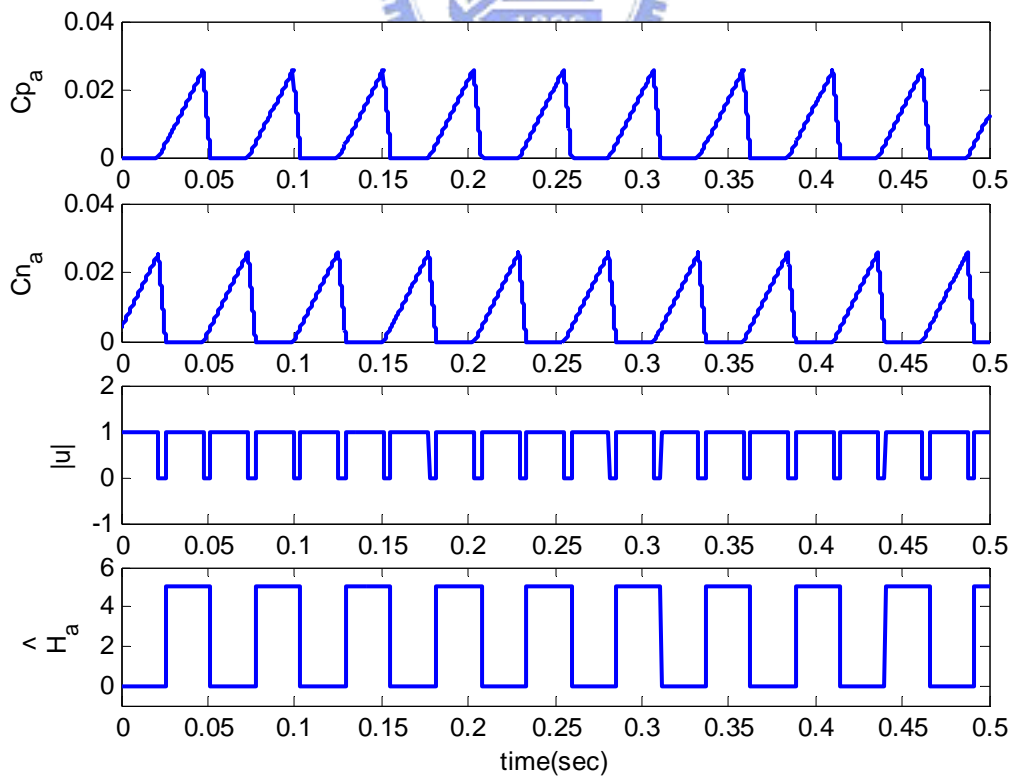


Fig.6.9 Sensorless control performance at high angular velocity (II)

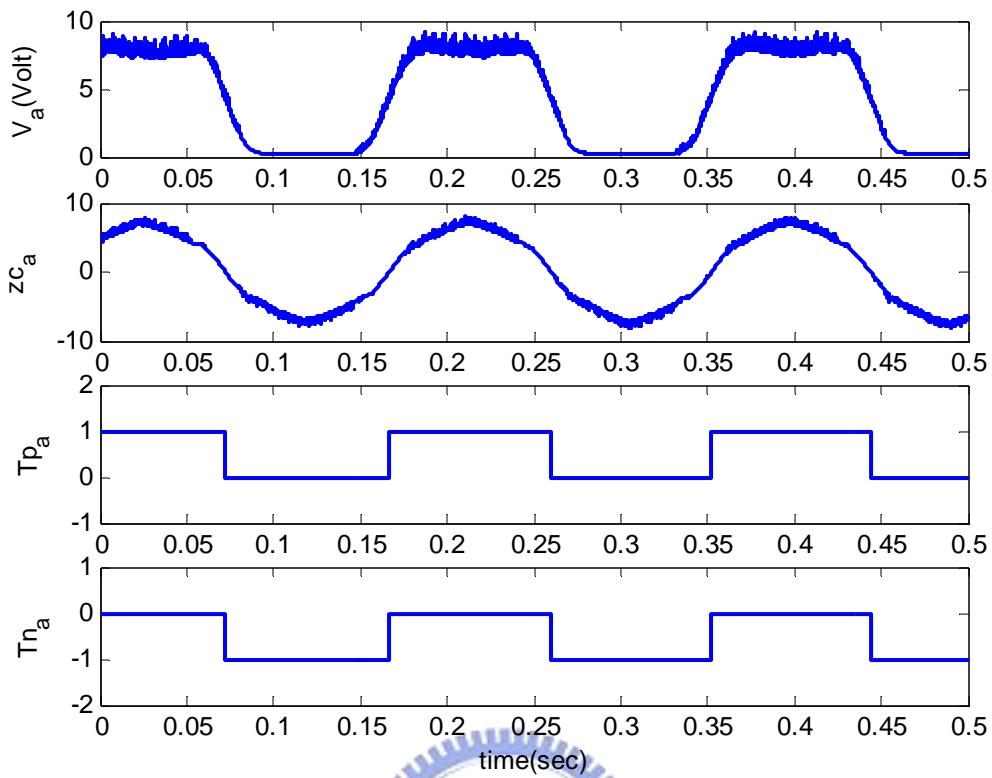


Fig.6.10 Sensorless control performance at low angular velocity (I)

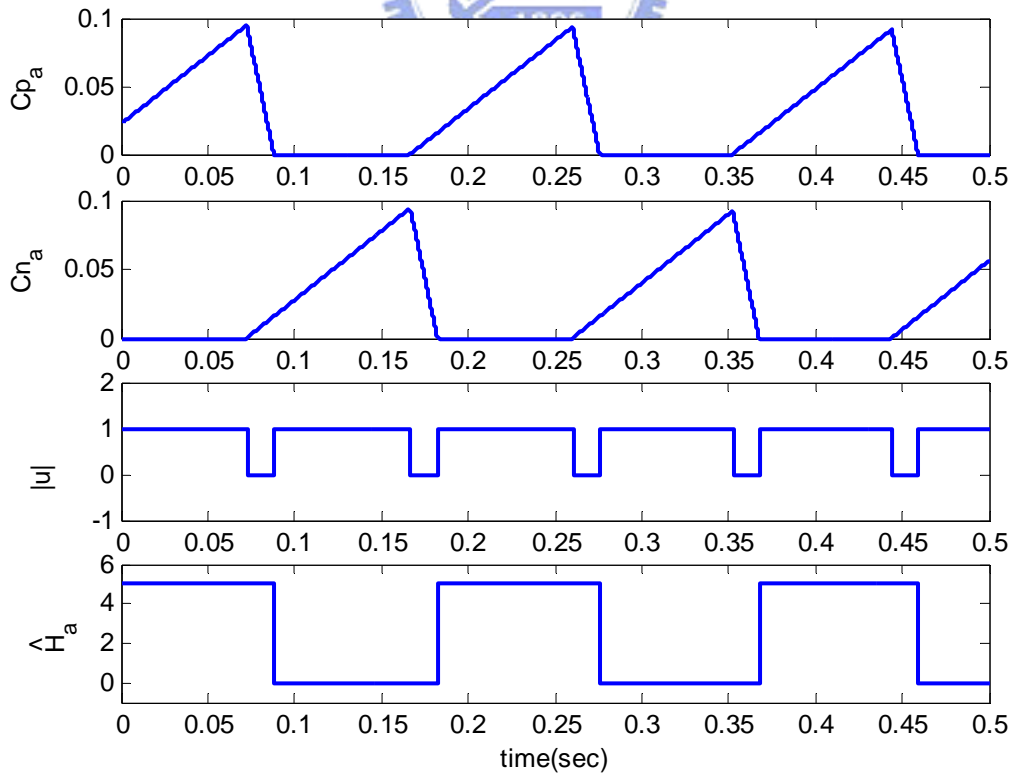


Fig.6.11 Sensorless control performance at low angular velocity (II)

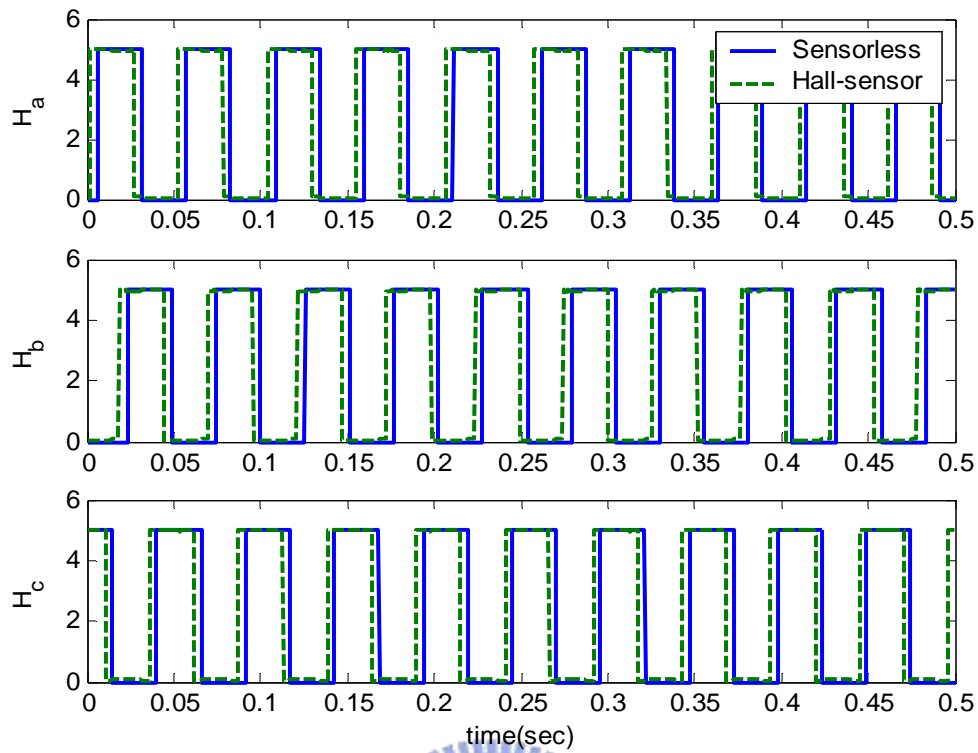


Fig.6.12 Comparison of the sensorless signals and conventional Hall-effect signals at high angular velocity

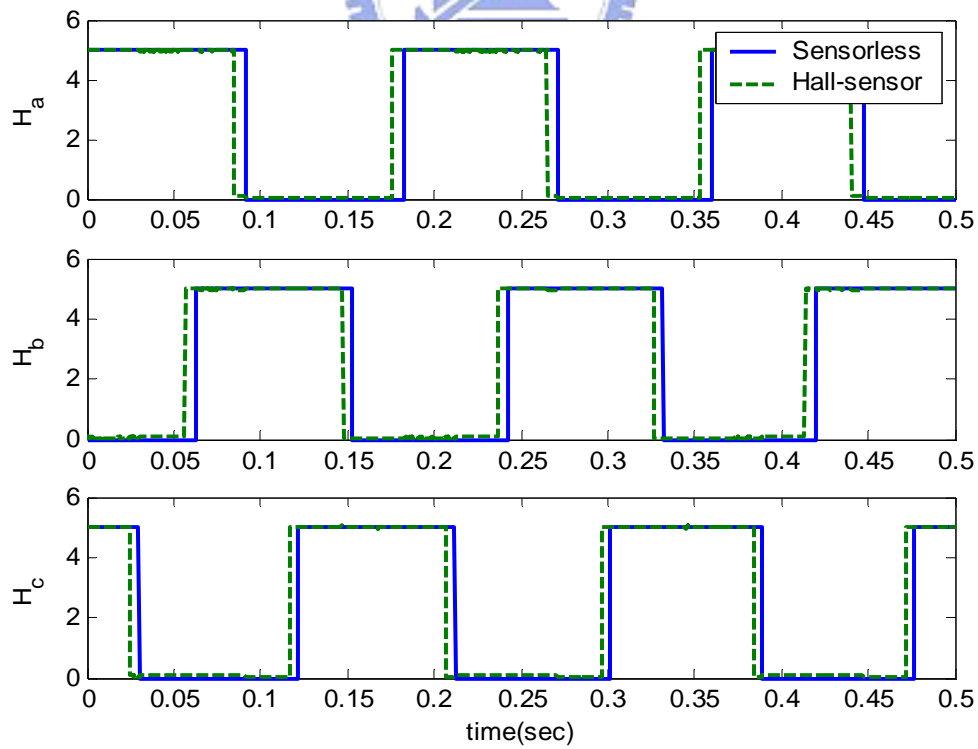
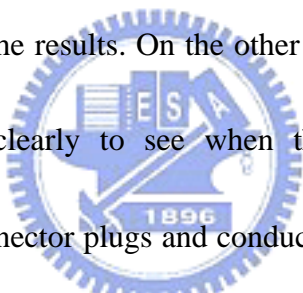


Fig.6.13 Comparison of the sensorless signals and conventional Hall-effect signals at low angular velocity

6.2 Experimental results of the start-up procedure

The start-up algorithm for initial position detection has been verified in Chapter 4.

Fig.6.14 shows the six current responses when the rotor is at standstill in a certain position. A voltage pulse is applied for all six segments, respectively, of an electrical cycle during $500\mu s$, to detect the stationary position of a rotor. The current is measured by three current sensors LP-25P, which is directly getting the current information from the motor. However, the residue in the magnetic field would affect the measured current responses. Thus, the longer distance of each pulse or import the inverse current will improve the results. On the other hand, the current noise which is chattering between ± 0.1 is clearly to see when the current is zero due to the electromagnetic interface, connector plugs and conducting wires. But the noises would not affect the detecting result since the detected current responses are large enough.



Besides, based on the polarity of ddi in Table 4.2 and Fig.4.5, the relative position of a rotor is found to be between 0° to 60° with sector 0 (see Table 4.3).

Then set up the command signal with a counter as shown in Fig.6.15. In addition, take the initial sector as the initial value in the counter, and the period of pulse generator will depend on the desired angular velocity when the motor is start-up. The period can refer to Table 4.4. Fig.6.16 shows the modified open-loop start-up form sector 0. Since the torque of the BLDC motor is very high and the back-EMFs are hard

to detect at very low angular velocity, there exists the jump position at starting in the Back-EMF detected sector. But the right direction rotating is produced. Fig.6.17 shows the difference between command sector and Back-EMF detected sector. This figure could be represented that the Back-EMF could be detected after about 2 second because the difference sector position is small than 1.

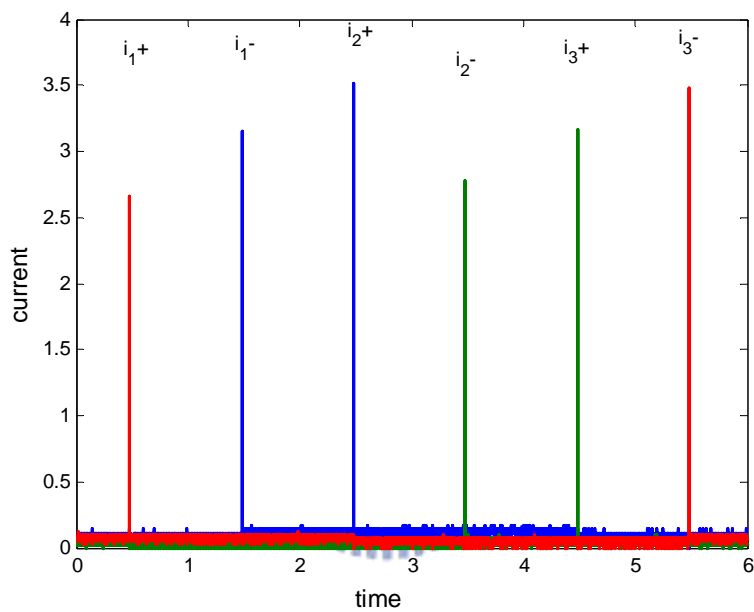


Fig.6.14 Measured the six current responses of an stationary rotor

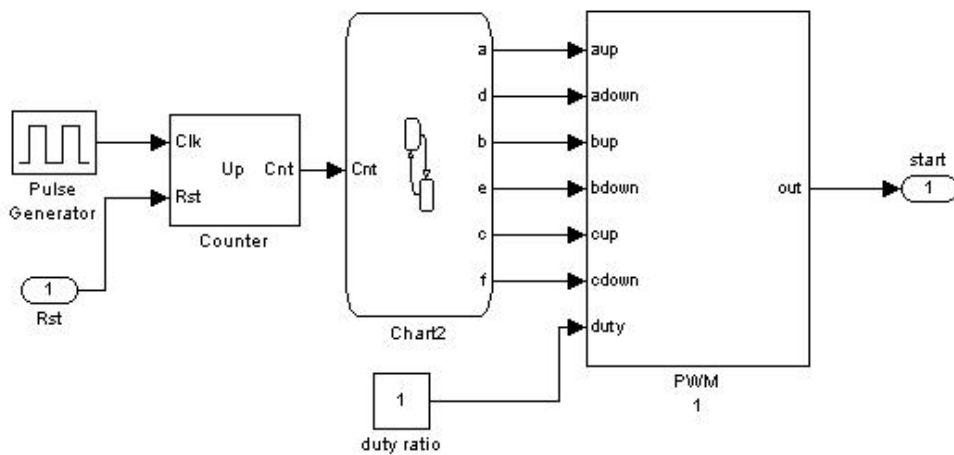


Fig.6.15 The block diagram of start-up procedure

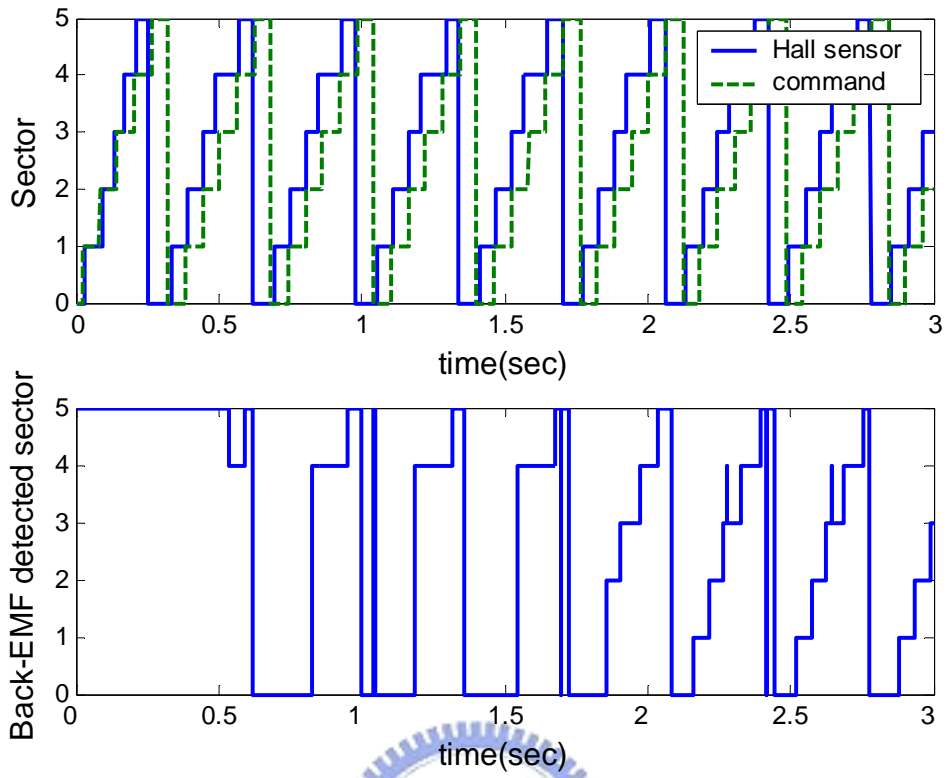


Fig.6.16 The modified open-loop start-up from sector 0

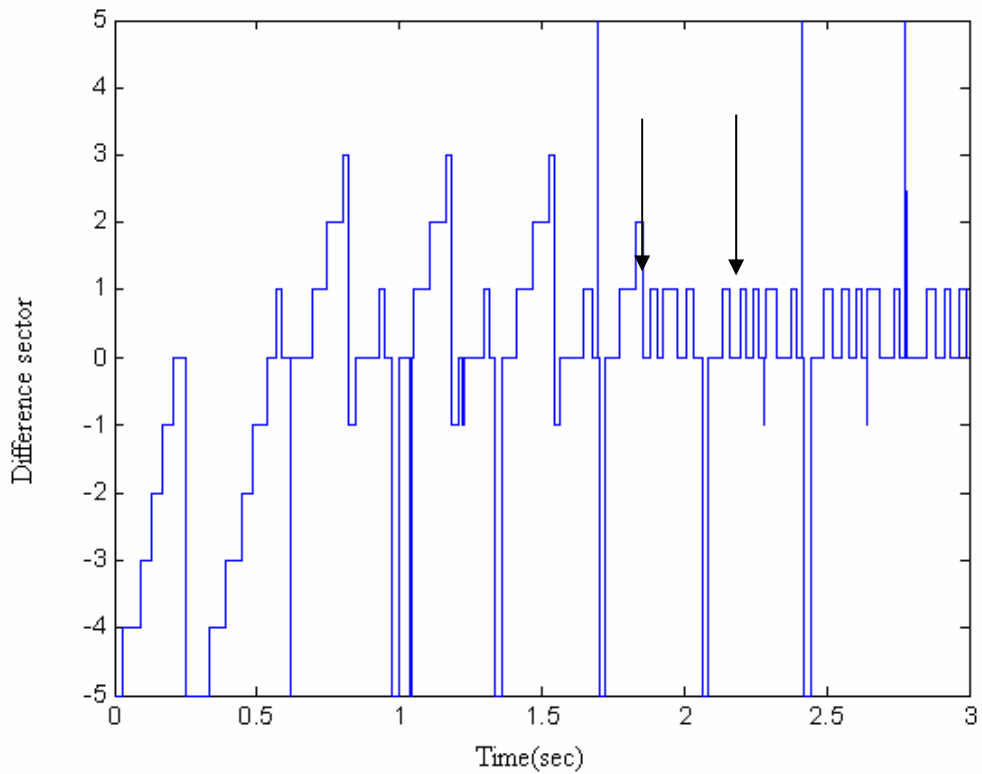


Fig.6.17 The difference between command sector and Back-EMF detected sector

Besides, the switch condition from the open-loop start-up mode to the sensorless commutation mode will be presented as follows. Fig.6.18 will show the block diagram of the whole sensorless system and the switch condition signal with 0 for start-up mode and 1 for commutation mode. In Fig.6.18 (b), the counter is set for detecting the *diff_on* signal. Once the difference sector is larger than 2 and smaller than 4 during the 0.5 sec, this counter will be reset and the switch signal is still 0 until another period which the *diff_on* signal maintained 0 for 0.5 sec.

Fig.6.19 and Fig.6.20 will show the experimental results of the motor from standstill to commutation mode at low angular velocity. Fig.6.21 and Fig.6.22 will show the results from standstill to commutation mode at high angular velocity.



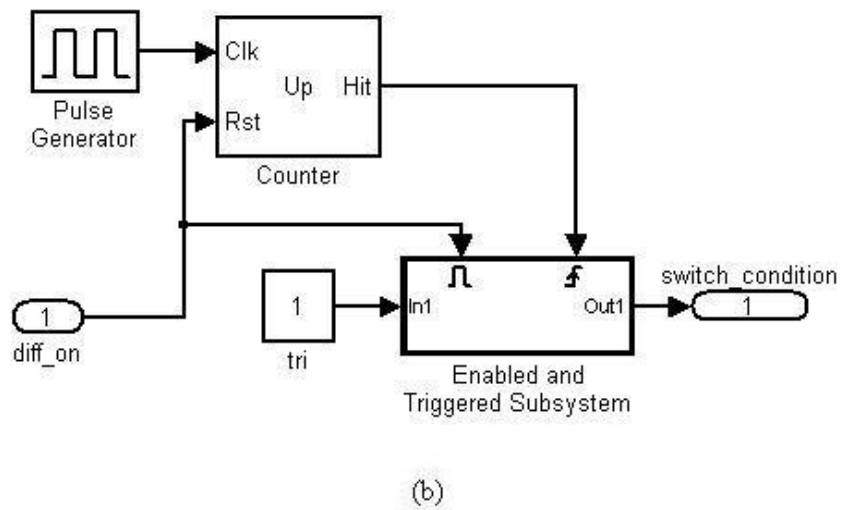
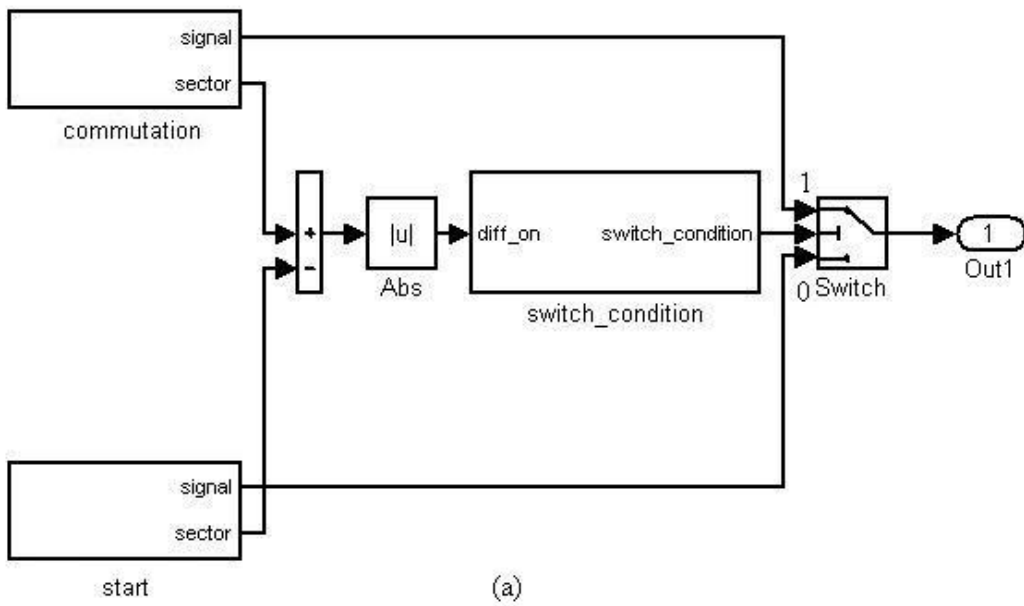


Fig.6.18 (a) The block diagram of the whole sensorless system and (b) the switch condition signal

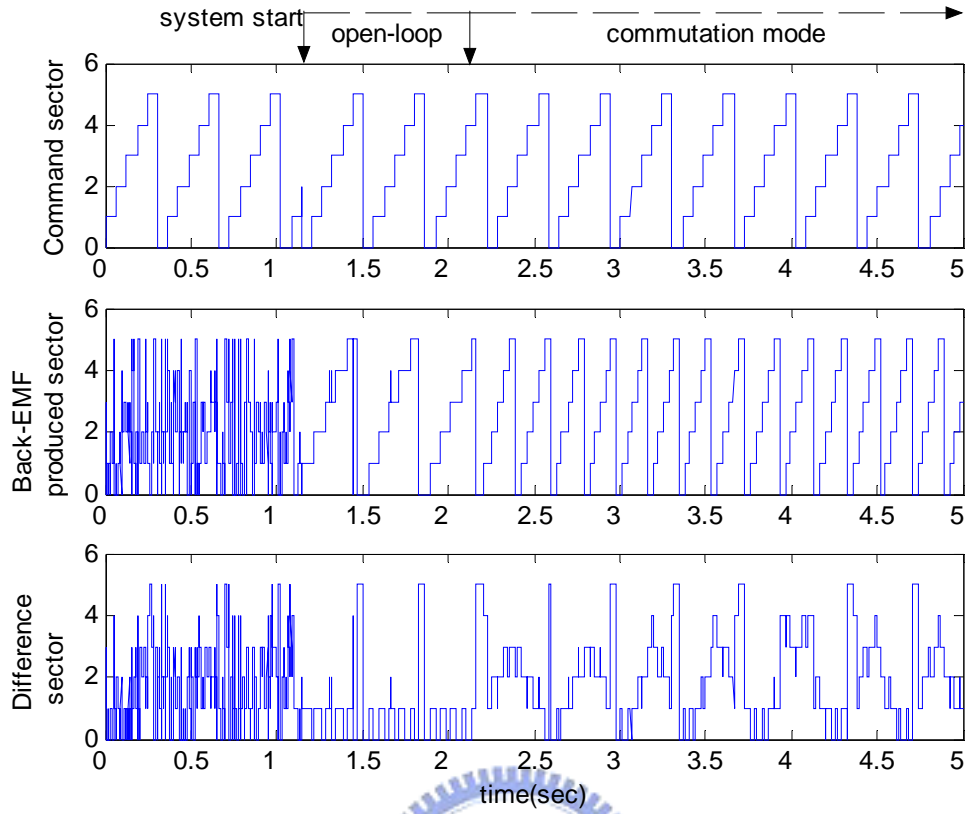


Fig.6.19 Results from standstill to commutation mode at low angular velocity (I)

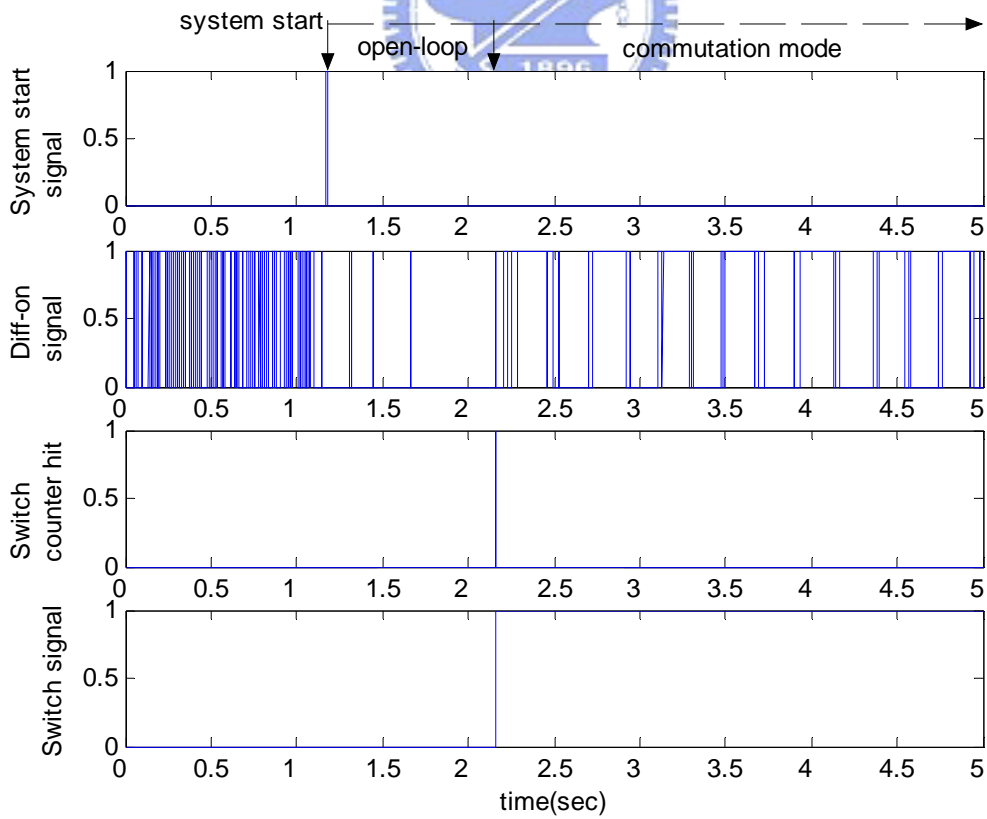


Fig.6.20 Results from standstill to commutation mode at low angular velocity (II)

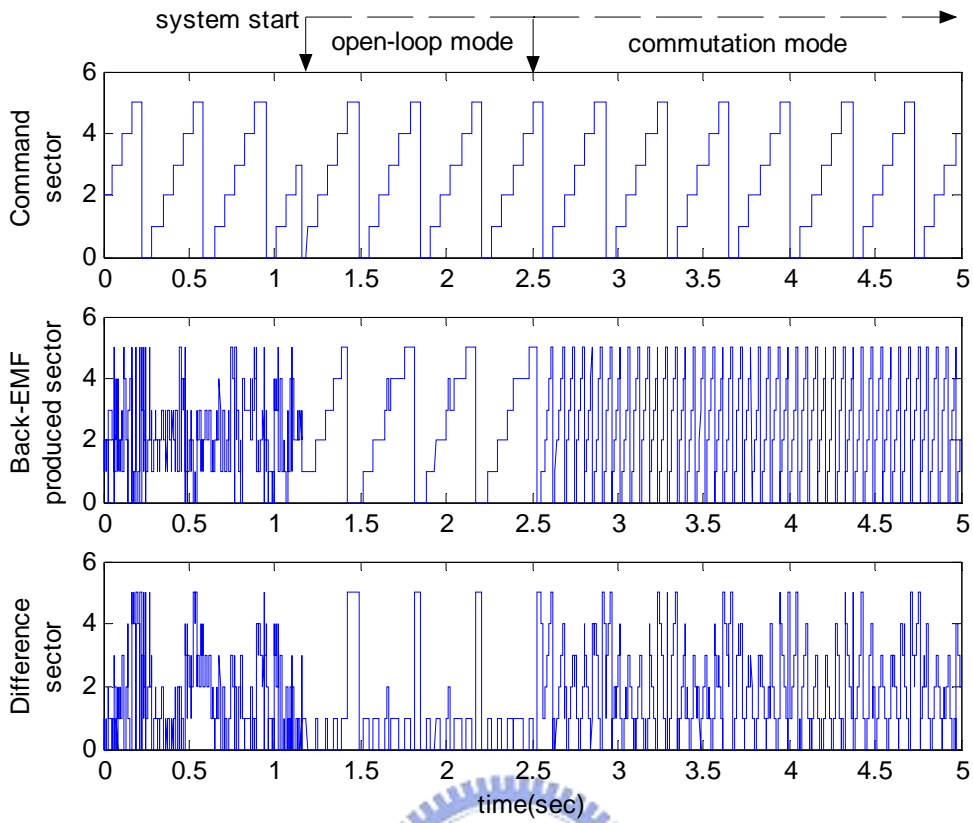


Fig.6.21 Results from standstill to commutation mode at high angular velocity (I)

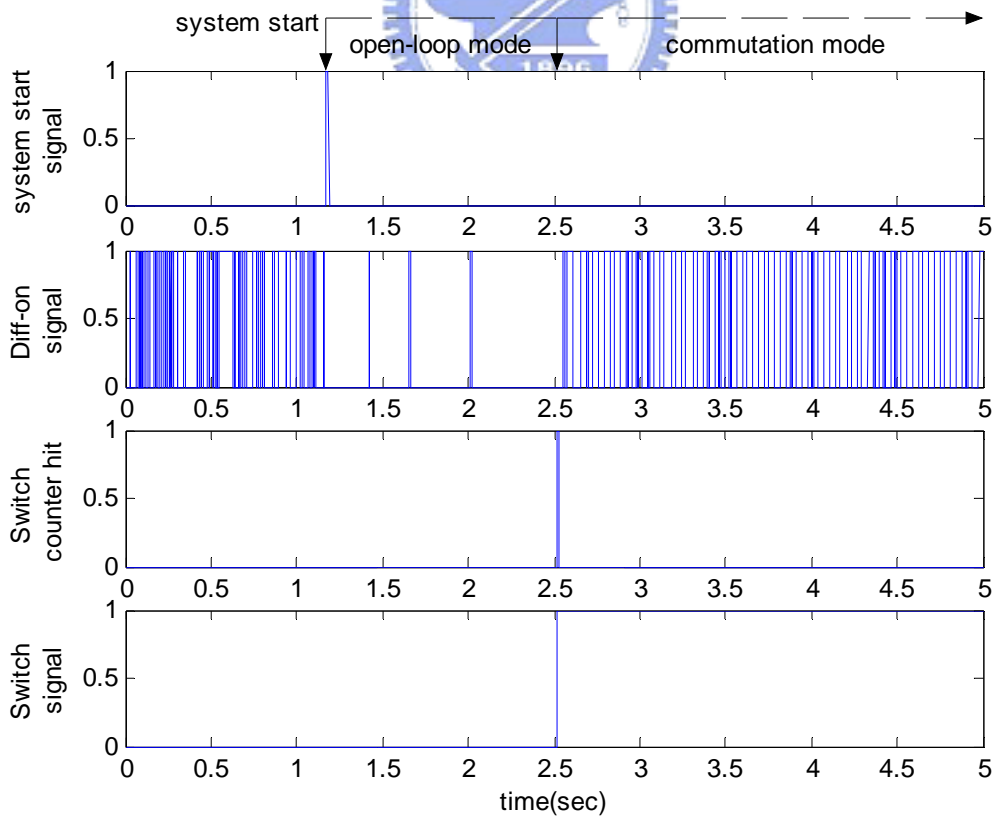


Fig.6.22 Results from standstill to commutation mode at high angular velocity (II)

Chapter 7

Conclusions

This thesis has analyzed and then realized a sensorless drive for the BLDC motor. The proposed sensorless control algorithm is implemented in a real-time motor drive, and is shown successful through the experimental results.

To identify the initial rotor position of a BLDC motor, a method is presented based on the inductance variation. Once the initial rotor position is attained, the motor can be driven from standstill effectively by a modified open-loop method even though the back-EMFs could not be exactly detected owing to the noises near zero-crossing point. After the BLDC motor starts, it is required to detect the commutation instants in phase, which is implemented by a back-EMF based position estimated method. This position estimated method adopts the conventional frequency-independent phase shifter and an additional low-pass filter designed for detecting the zero-crossing points at low angular velocity.

On the other hand, in order to improve the performance, the implementation of hardware using DSP card is worth proceeding since the sampling rate can reach 120 MIPS. In this way, the current will be measured more precisely such that the initial position will be detected more accurately. Besides, the sensorless control at a very low speed is not suitable to use the back-EMF based position estimated method because the

current is discontinuous in a low angular velocity 10 rpm. Therefore, the discontinuity should be taken into account to improve the performance while current model based sensorless approaches are adopted.

In summary, the experimental results verify that the sensorless strategy is a useful alternative for applications that require high efficiency, high performance, and robust BLDC motor drives.



Reference

- [1] K. Y. Cheng and Y. Y. Tzou, "Design of a Sensorless Commutation IC for BLDC Motors," *IEEE Transactions on Power Electronics*, vol.18, no.6, pp.1365-1375, November 2003.
- [2] J. Shao, D. Nolan, and T. Hopkins, "Improved direct back EMF detection for sensorless brushless DC (BLDC) motor drives," in *Proc. IEEE-APEC Conf.*, 2003, pp.300-305.
- [3] D. H. Jung and I. J. Ha, "Low-cost sensorless control of brushless DC motors using frequency-independent phase shifter," *IEEE Transactions on Power Electronics*, vol.15, no.4, pp.744-752, July 2000.
- [4] B. Terzic and M. Mohan, "Design and Implementation of the Extended Kalman Filter for the Speed and Rotor Position Estimation of Brushless DC Motor," *IEEE Transactions on Industrial Electronics*, vol.48, no.6, pp. 1065-1073, December 2001.
- [5] J. C. Moreira, "Indirect Sensing for Rotor Flux Position of Permanent Magnet AC Motors Operating Over a Wide Speed Range," *IEEE Transactions on Industry Applications*, vol.32, no.6, pp.1394-1401, November 1996.

- [6] S. Ogasawara and H. Akagi, "An approach to position sensorless drive for brushless dc motors," *IEEE Tran. Industry Applications*, vol. 27, no. 5, pp. 928-933, Sep. /Oct. 1991.
- [7] S. J. Kang and S. K. Sul, "Direct torque control of brushless DC motor with nonideal trapezoidal back EMF," *IEEE Trans. Power Electron.*, vol.10, no. 6, pp.796-802, Nov. 1995.
- [8] P. Pillay and R. Krishnan, "Modeling, simulation, and analysis of permanent-magnet motor drives, part II: The brushless dc motor drive," *IEEE Trans. Industry Applications*, vol. 25 no. 2 pp.274-279 Mar./Apr. 1989.
- [9] P. Pillay and R. Krishnan, "Modeling, simulation, and analysis of permanent-magnet motor drives, part I: The permanent magnet synchronous motor drive," *IEEE Trans. Industry Applications*, vol. 25 no.2 pp.265-273 Mar. /Apr. 1989.
- [10] G. H. Jang, J. H. Park and J. H. Chang, "Position detection and start-up algorithm of a rotor in a sensorless BLDC motor utilizing inductance variation," *IEE Proc.-Electr. Power Applicat.*, vol. 149, no. 2, pp.137-142, March 2002.
- [11] M. Tursini, R. Petrella, and F. Parasiliti, "Initial Rotor Position Estimation Method for PM Motors," *IEEE Tran. Industry Application*, vol.39, no.6, pp.1630-1640, Nov. /Dec. 2003.

- [12] J. P. Johnson, M. Ehsani, and Y. Guzelgunler, "Review of Sensorless Methods for Brushless DC," *IEEE Trans. Industry Applications Conference, Thirty-Fourth IAS Annual Meeting*, vol. 1, pp.143-150, 3-7 October 1999.
- [13] T. Yoon, "Stator design consideration of a Brushless DC motor for robust rotor position detection in inductive sense start-up," *IEEE Trans. Magnetic*, vol. 42, no. 3, March 2006.
- [14] IR2110/2113(S) Data Sheet No.PD60147-O from *International Rectifier Company*.
- [15] PCI-6024E Data Sheet from *National Instruments*.
- [16] IRF640N, HEXFET[®] Power MOSFET, Data Sheet No.PD94006 from *International Rectifier Company*.
- [17] "PWM Management for BLDC Motor Drives Using The ST72141," AN1129 Application Note, STMicroelectronicsInc.
- [18] 孫清華, 黃昌圳, *最新直流無刷馬達*, 全華, 2001
- [19] 鄭光耀, 無刷直流馬達無感測控制方法之研究與 DSP 實現技術之發展, 國立交通大學電機與控制工程學系, 博士論文, 2003.
- [20] 林穎燦, 無刷直流馬達無感測換相控制 IC 之規劃與設計, 國立交通大學電機與控制工程系, 碩士論文, 2002.

[21] 林瀚宏, 無刷直流馬達之分析與無感測器驅動之建模, 國立交通大學電機與控制工程系, 碩士論文, 2004.

[22] 吳欣達, 順滑模態估測器應用於無感測無刷直流馬達之速度控制, 國立交通大學電機與控制工程系, 碩士論文, 2005.



Appendix A

Position detection and start-up algorithm of BLDC motors by using inductance variation

A method of identifying the rotor position of a BLDC motor and driving a motor smoothly from standstill without any position sensors is presented [18]. This is done by monitoring the current responses to the inductance variation on the rotor position. Furthermore, the start-up algorithm also proposed to detect the next commutation timing by injecting a current pulse into six segments of an electrical cycle. In this section, this start-up method proposed by G. H. Jang, J. H. Park and J. H. Chang will be introduced in detail.



A.1 Position detection

The six segments of an electrical cycle are shown in Table A.1. In (3-28)-(3-32) represents that the phase current shows a different response depending on the inductance variation, which is determined by the relative position of a rotor and the direction of the current. Thus, the position information can be obtained by monitoring the phase current i^+ and i^- in an appropriate time interval.

Table A.1 Six segments of an electrical cycle

Segment	Symbol of current
\overline{AB}	i_1^+ (i)
\overline{BA}	i_1^- (ii)
\overline{CA}	i_2^+ (iii)
\overline{AC}	i_2^- (iv)
\overline{BC}	i_3^+ (v)
\overline{CB}	i_3^- (vi)

In Fig.A.1, the current responses of the well-known six segments are calculated with the determined inductance in an appropriate interval of electrical degrees. Observing Fig.A.1, it should be noted that the polarity of the difference between the positive current and negative current, Δi_n , changes every 180 electrical degrees. Furthermore, the inherent differences with 120 electrical degrees exist in any two phases such that the polarity of one of three changes every 60 electrical degrees, which can provide the position information, as shown in Fig.A.2. However, the position information from Δi_n is not proper to drive a motor. The polarity of the difference between $\Delta i_n - \Delta i_m$, $\Delta \Delta i_k$, can be effectively used to identify the rotor position due to it includes the information of the polarity of the difference between two back-EMF used in six-step drive. The polarity of one of three $\Delta \Delta i_k$ changes every 60 electrical degrees with 30 electrical degrees shift compared with the variation of Δi_n , as shown in Fig. A.3 and Table A.2. Thus, the initial rotor position can be detected by monitoring

the polarity of Δi_k , after each of six segments has been supplied a voltage pulse with a $20 \mu s$ period.

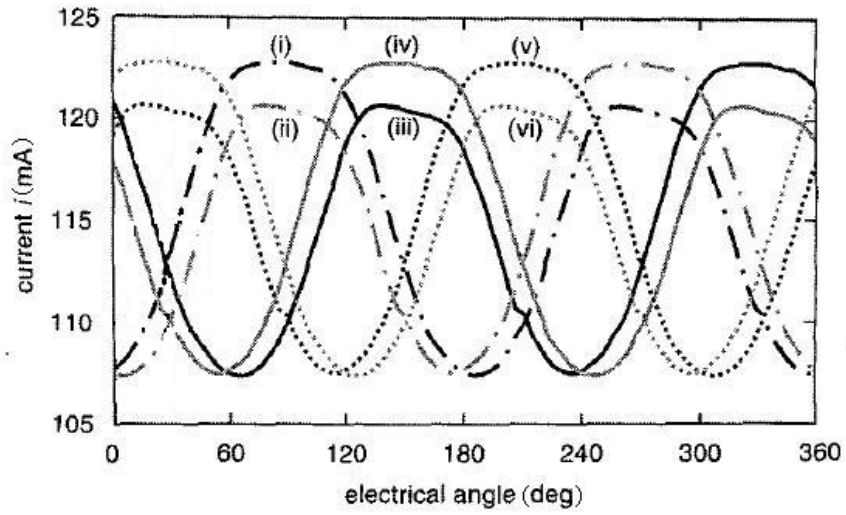


Fig. A.1 The current responses of the well-known six segments

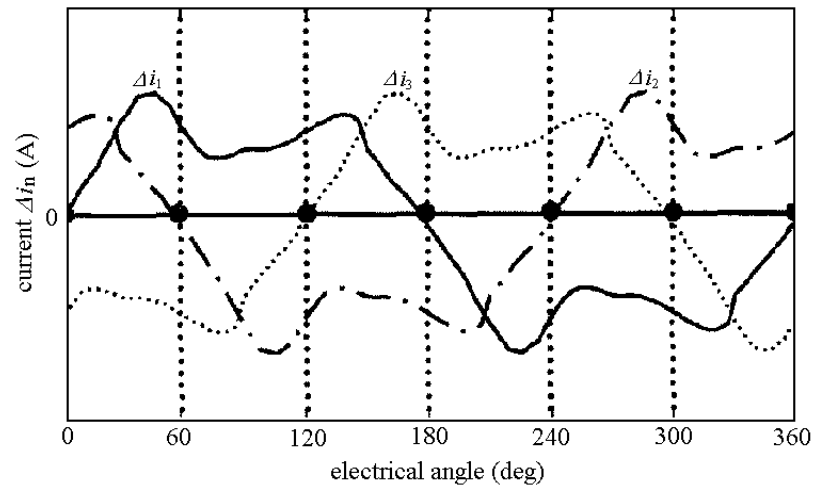


Fig. A.2 The differences between the current i_n^+ and i_n^-

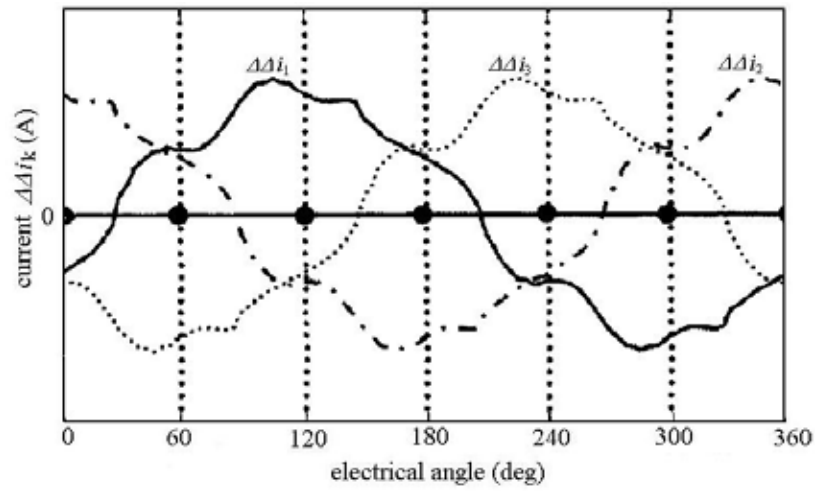


Fig. A.3 The differences between the current Δi_n

Table A.2 Polarity of $\Delta\Delta i_k$ on rotor position

Electrical position	$\Delta\Delta i_1$	$\Delta\Delta i_2$	$\Delta\Delta i_3$
$30^\circ \sim 90^\circ$	+	+	-
$90^\circ \sim 150^\circ$	+	-	-
$150^\circ \sim 210^\circ$	+	-	+
$210^\circ \sim 270^\circ$	-	-	+
$270^\circ \sim 330^\circ$	-	+	+
$330^\circ \sim 30^\circ$	-	+	-

A.2 Start-up algorithm

Once the stationary position of a rotor is identified, the correct phases of a BLDC motor are energized to produce the maximum torque. However, since six pulses cannot be inject during a commutation period as the motor moving quickly and some of these pulses generate negative torque by using position detection, the start-up algorithm is needed to detect the next commutation timing.

Consider the torques produced by the six segments with respect to the electrical angle as shown in Fig.A.4, in which every two phases out of three are energized in the positive or negative direction. Except the exciting segment which produces the maximum torque, there are still two segments to produce the torque with same direction in every commutation period. It should be noted that the increasing one is the next excitation. In other words, the increasing segment should replace the original exciting segment to be the new exciting segment while the torque produced by the increasing segment is larger than the torque produced by the original exciting segment. For example, the phases \overline{AB} should be switched o the phases \overline{AC} when a rotor passes S_{CB} . The phases \overline{AB} is excited when the initial position is detected as 0~30 electrical degrees. It means that the exciting phases is \overline{AB} and increasing phases is \overline{AC} . In Fig.A.5, P_{phase} and P_{pulse} correspond to the long and short pulses to energize the current the current phase \overline{AB} and the next commutation \overline{AC} before the rotor passes

S_{CB} . Therefore, the next excitation can be determined while the current of \overline{AC} is larger than \overline{AB} the current of. The composition of the exciting phases and increasing phases with respect to electrical angle is shown in Table A.3. The pulse train can accelerate the motor to medium speed. Once the motor produced sufficient back-EMF, the sensorless algorithm of the BLDC motor is switched to a back-EMF position detection method by using the zero-crossing of the back-EMF.

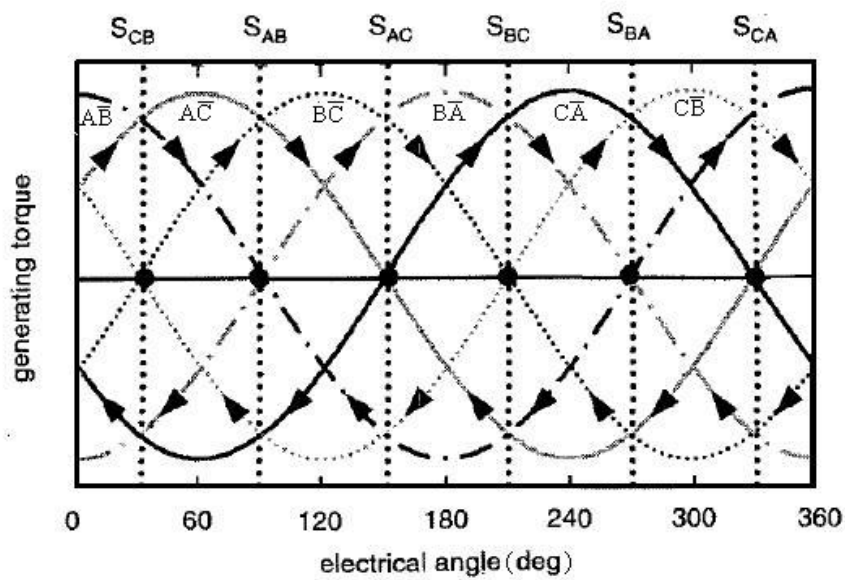


Fig.A.4 The torque generation of the six segments

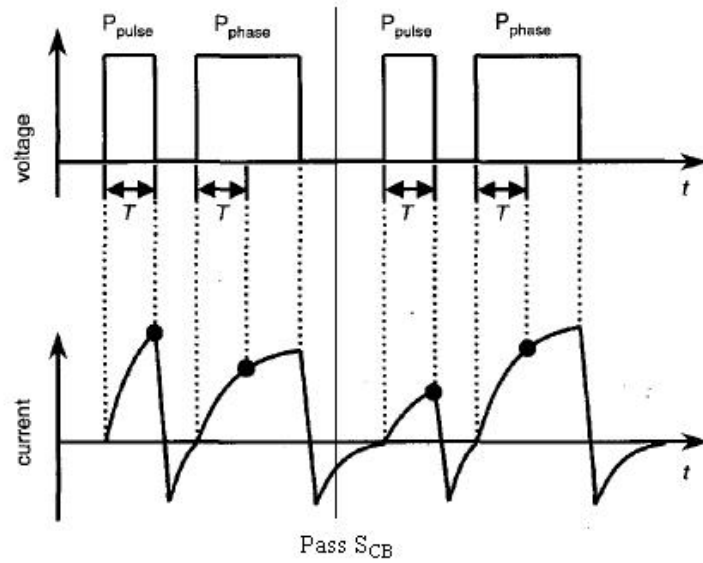


Fig.A.5 The pulse train and its response

Table A.3 The exciting and increasing segment at electrical angle

Electrical position	Exciting	Increasing
$30^\circ \sim 90^\circ$	$A\bar{C}$	$B\bar{C}$
$90^\circ \sim 150^\circ$	$B\bar{C}$	$B\bar{A}$
$150^\circ \sim 210^\circ$	$B\bar{A}$	$C\bar{A}$
$210^\circ \sim 270^\circ$	$C\bar{A}$	$C\bar{B}$
$270^\circ \sim 330^\circ$	$C\bar{B}$	$A\bar{B}$
$330^\circ \sim 30^\circ$	$A\bar{B}$	$A\bar{C}$